Revised version June 20, 2023

Uncovering the Critical Factors that Enable Extractive Desulfurization of Fuels in Ionic Liquids and Deep Eutectic Solvents from Simulations

Kun Yue and Orlando Acevedo*

Department of Chemistry, University of Miami, Coral Gables, Florida 33146

E-mail: orlando.acevedo@miami.edu

Submitted April 21, 2023

Abstract: Environmental regulatory agencies have implemented stringent restrictions on the permissible levels of sulfur compounds in fuel to reduce harmful emissions and improve air quality. Problematically, traditional desulfurization methods have shown low effectiveness in the removal of refractory sulfur compounds, e.g., thiophene (TS), dibenzothiophene (DBT), and 4-methyldibenzothiophene (MDBT). In this work, molecular dynamics (MD) simulations and free energy perturbation (FEP) have been applied to investigate the use of ionic liquids (ILs) and deep eutectic solvents (DESs) as efficient TS/DBT/MDBT extractants. For the IL simulations, the selected cation was 1-butyl-3-methylimidazolium [BMIM], and the anions included chloride [Cl], thiocyanate [SCN], tetrafluoroborate [BF_4], hexafluorophosphate [PF_6], and bis(trifluoromethylsulfonyl)amide [NTf_2]. The DESs were composed of choline chloride with ethylene glycol (CCEtg) or with glycerol (CCGly). Calculation of excess chemical potentials predicted the ILs to be more promising extractants with energies lower by 1-3 kcal/mol compared to DESs. Increasing IL anion size was positively correlated to enhanced solvation of S-compounds, which was influenced by energetically dominant solute-anion interactions and favorable solute-[BMIM] π-π stacking. For the DESs, the solvent components offered a range of synergistic, yet comparatively weaker electrostatic interactions that included hydrogen bonding and cation-π interactions. An in-depth analysis of the structure of IL and DES systems is presented, along with a discussion of the critical factors behind experimental trends of S-compound extraction efficiency.

Introduction

The United States Environmental Protection Agency (EPA) mandated a 97 percent reduction in the sulfur content of diesel fuel from 500 parts per million (ppm) to 15 ppm over 15 years ago.[1] Phased-in over years, the EPA expects both vehicles and the entire nonroad diesel engine inventory to comply with these new standards by 2030.[2] The environmental benefits are significant by reducing harmful emissions by more than 90% or the equivalent of eliminating air pollution from 13 million trucks per year.[1] Positive impacts for public health include reduced cases of chronic and acute bronchitis and asthma.[3, 4] However, the economic impact of ultra-low sulfur diesel (ULSD) production has meant an increase in cost to refiners, and therefore, consumers. Conventional desulfurization techniques are not well equipped to handle the deep desulfurization (10-15 ppm S) required.[5, 6] In addition, the strong chemical absorption of sulfur can cause poisoning and deactivation for most metal catalysts, while the accumulation of sulfur compounds during the catalytic process can corrode equipment.[2, 7, 8]

The most mature and widely applied technology is hydrodesulfurization (HDS), where the sulfur-containing compounds are catalytically converted into H_2S in the presence of H_2 at high pressure and temperatures.[9, 10] The H_2S is then removed by amine washing using the Claus process. The harsh production conditions require a significant investment in equipment, incur large operating costs, and consumes a large amount of hydrogen and energy. Most importantly, HDS shows low effectiveness in the removal of heterocyclic sulfur compounds (also referred to as refractory sulfur compounds[11]), such as thiophene (TS), benzothiophene (BT), dibenzothiophene (DBT), and 4-methyldibenzothiophene (MDBT) due to their high stability and steric hindrance (Scheme 1). Increasing the severity of the HDS process conditions and using expensive catalysts can promote further desulfurization,[12-14] but results in undesirable outcomes including a decrease in the octane rating, a rise in coke formation, and a decreased catalyst lifespan.[15] Therefore, alternative desulfurization technologies are desirable.[16, 17]

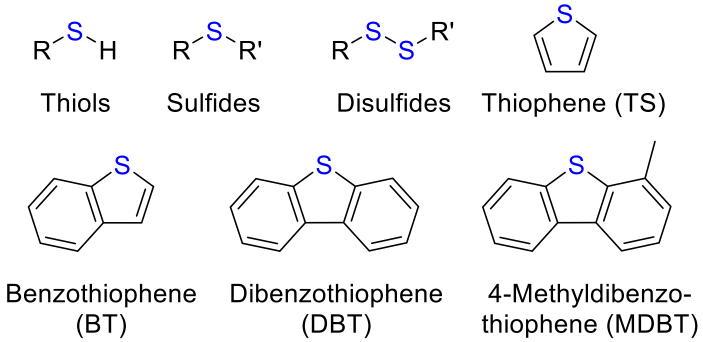

Scheme 1. Sulfur compounds present in fuel and diesel oil.

Non-HDS technologies are available and primarily consist of biological desulfurization (BDS), adsorption desulfurization (ADS), oxidation desulfurization (ODS), and extraction desulfurization (EDS). Detailed reviews for each desulfurization technology are available elsewhere, but a summary of the four methods is provided here. (1) BDS employs microorganisms to decompose sulfur compounds in fuels;[18-20] several bacterial species have been applied, including *Pseudomonas, Rhodococcus*, and *Gordonia*.[21] Despite the attractive benefits, such as lower costs and smaller greenhouse gas emissions, BDS is at present not viable for commercial application due to a relatively slow desulfurization rate compared to chemical reactions, a large biomass requirement, and a similarity in mechanism between the biochemical desulfurization pathway and hydrocarbon degradation. (2) The ADS methodology features adsorbents that allow sulfur compounds to adhere to a porous substrate without the need for chemical reactions.[22] The most significant advantages of ADS are the rapid adsorption process, mild operating temperature, and the theoretically achieved low sulfur levels. However, the development of low-cost industrial-scale adsorbents with a high adsorption capacity, good regenerative properties, and superior selectivity has been challenging. (3) ODS is a two-step technology where sulfur compounds are oxidized to their respective sulfoxides or sulfones, which are then removed by extraction adsorption or distillation.[23, 24] While ODS has major advantages including mild pressures and temperatures, low cost, and no H_2 consumption, the oxidants/catalysts utilized need to selectively react with the sulfur compounds to avoid fuel quality degradation. (4) EDS is the final desulfurization method discussed here and is one of the most attractive technologies as it has the same benefits as ODS with no catalyst required.[25] The sulfur compounds are selectively removed during the process using extractant solvents without reacting with the desirable hydrocarbons. However, conventional extractants, including DMF, DMSO, and CH_3CN, have severe drawbacks such as volatility, toxicity, poor selectivity, and contamination.[26] Hence, the use of environmentally friendly and cost-effective alternative solvents, such as imidazolium-based ionic liquids (ILs) and deep eutectic solvents (DESs), for extraction processes have a gained significant interest over the years.[27]

Pioneering work by Jess and co-workers in 2001 showed that refractory sulfur compounds could be extracted efficiently from diesel fuel using ionic liquids.[28] Their study featured room temperature molten salts composed of 1-alkyl-3-methylimidazolium cations, [RMIM] where R = E for ethyl, B for butyl, and O for octyl, and variety of diffuse inorganic and organic anions (Scheme 2). Early follow-up investigations by Jess[29] and others have been described in reviews.[25, 30, 31] Since then, hundreds of studies featuring the use of ILs in desulfurization technologies have been published.[32-34] Many of these experimental studies have primarily focused on liquid-liquid equilibrium (LLE) data testing for binary or ternary mixtures, the measurement of activity coefficients at infinite dilution (γ_i^∞) and of extraction related thermodynamics properties. Beginning in 2003, Abbott et al. reported a series of IL analogs they coined “deep eutectic solvents” that share many similarities with the room-temperature molten salts.[35, 36] DESs are binary or ternary mixtures of hydrogen bond acceptors (HBAs) and neutral hydrogen bond donors (HBDs) with decreased melting temperatures relative to the isolated compounds (Scheme 3).[37] For example, an extremely popular DES called reline is composed of choline chloride (ChCl) and urea in a molar ratio of 1:2 that results in a melting point of 12 °C, which is significantly lower than that of ChCl (302 °C) and urea (133 °C) individually.[35, 36] In 2013, the Li group recognized that DESs can provide strong hydrogen bonding as a driving force in the EDS process and reported the first work incorporating DESs in fuel desulfurization.[38] Similar to ILs, experimental desulfurization studies using DESs have centered on LLE data of mixtures, the synthesis of new DESs, and measurements of relevant extraction properties.[39-42]

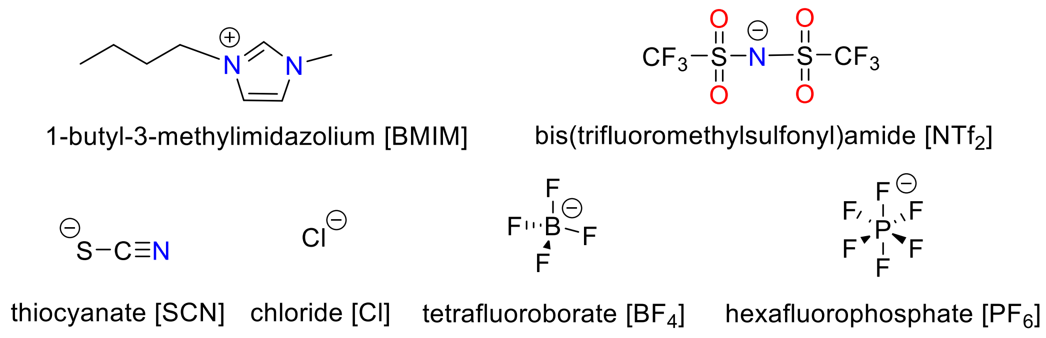

Scheme 2. Chemical structures of typical ionic liquid forming ions.

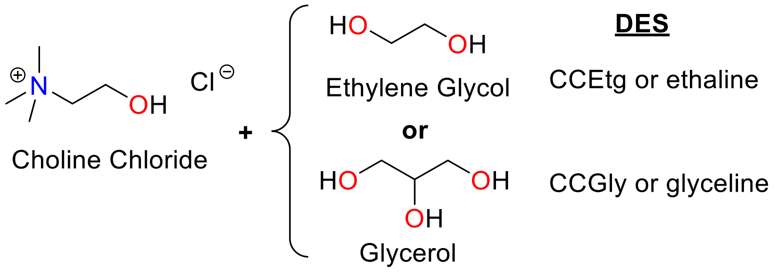

Scheme 3. The constituents of deep eutectic solvents CCEtg and CCGly.

Computational simulations have been utilized extensively to aid in the discovery of high-performance IL/DES-based extractants for sulfur removal.[43, 44] Multiple theoretical methods have been applied to investigate interactions between IL/DESs and sulfur compounds, predict the properties of IL/DESs-sulfur mixtures, and assist in the design and screening of different IL/DESs for extraction desulfurization. For example, computational methods that include the conductor-like screening model for realistic solvents (COSMO-RS),[45-48] quantum mechanics (QM),[33, 49] molecular dynamics (MD),[50, 51] and Monte Carlo (MC)[52] have provided significant insight into the desulfurization process. In this work, MD simulations have been performed to elucidate the intermolecular interactions responsible for the efficient extraction of the TS, DBT, and MDBT sulfur compounds (Scheme 1) using five different imidazolium-based ILs and two unique DESs. For the ionic liquids, the selected cation was 1-butyl-3-methylimidazolium [BMIM], and anions included chloride [Cl], tetrafluoroborate [BF_4], hexafluorophosphate [PF_6], thiocyanate [SCN], and bis(trifluoromethylsulfonyl)amide [NTf_2] (Scheme 2). Whereas the deep eutectic solvents were composed of choline chloride (ChCl) and the ethylene glycol and glycerol hydrogen bond donors in a 1:2 ChCl:HBD molar ratio to yield the CCEtg (ethaline) and CCGly (glyceline) DESs, respectively (Scheme 3). The above solvents were chosen due to their popularity in the literature, their high potential as sulfur extractants, and the availability of validated force field parameters. Radial, angular, and spatial distribution functions were used to analyze the interactions between solvents and cyclic sulfur compounds. In addition, the excess chemical potential of TS, DBT, and MDBT was computed in ILs/DESs using free energy perturbation (FEP) techniques.

Computational Methods

OPLS-AA Force Field. The nonpolarizable OPLS-AA force field (FF) uses a combination of intramolecular and intermolecular terms to compute the total energy of the system. The harmonic bond stretching and angle bending terms, the Fourier series for dihedral angles, and the intermolecular energies from Coulomb and 12-6 Lennard-Jones terms are provided in equations 1-4. The adjustable parameters are the force constants k, the r_o and θ_o equilibrium bond and angle values, Fourier coefficients V, partial atomic charges, q, and Lennard-Jones radii and well-depths, σ and ε. In this work, IL FF parameters were taken from ±0.8 charge-scaled OPLS-2009IL[53, 54] and the virtual site OPLS-VSIL[55-57] (Tables S1-S4) and the DES FF parameters came from OPLS-DES.[58, 59] All FF parameters are available to download at https://github.com/orlandoacevedo/IL and https://github.com/orlandoacevedo/DES as preformatted GROMACS files. The cyclic sulfur compounds OPLS-AA parameters were generated using the 1.14*CM1A-LBCC charge model through the LigParGen web server.[60]

$$E_{bonds} = \sum_i k_{r,i}(r_i - r_{0,i})^2 \tag{1}$$

$$E_{angles} = \sum_i k_{\theta,i}(\theta_i - \theta_{0,i})^2 \tag{2}$$

$$E_{torsion} = \frac{1}{2}\sum_i[V_{1,i}(1+\cos\phi_i) + V_{2,i}(1-\cos 2\phi_i) + V_{3,i}(1+\cos 3\phi_i) + V_{4,i}(1-\cos 4\phi_i)] \tag{3}$$

$$E_{nonbond} = \sum_i \sum_{j>i}\left\{\frac{q_i q_j e^2}{r_{ij}} + 4\varepsilon_{ij}\left[\left(\frac{\sigma_{ij}}{r_{ij}}\right)^{12} - \left(\frac{\sigma_{ij}}{r_{ij}}\right)^{6}\right]\right\} \tag{4}$$

Standard geometric combining rules, i.e., $\sigma_{ij} = (\sigma_{ii}\sigma_{jj})^{1/2}$ and $\varepsilon_{ij} = (\varepsilon_{ii}\varepsilon_{jj})^{1/2}$ were applied to the Lennard-Jones coefficients. Nonbonded interactions were calculated intermolecularly and for intramolecular atom pairs separated by three or more bonds. To apply the same parameters for both intra- and intermolecular interactions the 1,4-intramolecular interactions were reduced by a factor of 2.

Molecular Dynamics. Unbiased molecular dynamic (MD) simulations were carried out using the GROMACS 2018.2 software package.[61] Cubic boxes containing 500 ion pairs for ILs or 500 ChCl and 1000 HBDs for the DESs and 10 cyclic sulfur compounds were constructed with the Packmol program[62] with a specified length to reproduce the experimental density (Tables S5 and S6). Periodic boundary conditions and Particle-Mesh Ewald summations (default settings) were applied to both electrostatics and van der Waals interactions. The systems were minimized using a steepest descent algorithm for 5000 steps. Equations of motion were integrated using the leap-frog algorithm with a time step of 1 fs. A temperature value of 298 K was kept constant using velocity rescaling with a stochastic term (v-rescale) and a constant pressure of 1.0 bar was maintained with the Berendsen coupling during an isothermal-isobaric ensemble (NPT) simulation for 5 ns of equilibration for the IL systems or 10 ns for the DES systems. A time constant of 1.0 ps was used for temperature and pressure coupling. The default compressibility value of 4.5×10^{-5} bar^{-1} was applied for the barostat. All covalent bonds to hydrogen atoms were constrained using the LINCS algorithm and a cutoff range for the short-range electrostatics was set to 13 Å. Production runs were performed for an additional 50 ns. The radial distribution functions (RDFs), combined distribution functions (CDFs), and spatial distribution functions (SDFs) for the last 30 ns of the MD trajectories were computed using the TRAVIS program[63, 64] and plotted using Mathematica. Additionally, coordination numbers (N_{coord}) were calculated by integrating the area under the first center-of-mass RDF peak (r_{max}) up to its first minimum (r_{min}) using TRAVIS.

Excess Chemical Potential. One sulfur molecule (TS, DBT, or MDBT) was transferred into a solvent box consisting of ILs or DESs, which was regarded as infinite dilution, and the free energy perturbation (FEP)-MD computational procedure reported by Velarde-Salcedo *et al.* was utilized to compute excess chemical potentials, $\mu_i^{ex,\infty}$.[65] FEP simulations were carried out using the GROMACS 2021.6 version introduced to simulate the process, and then the energy was obtained through the Bennett's acceptance ratio method (BAR).[66] The same MD procedure discussed previously was used in the FEP-MD simulations with some changes noted below. The initial cubic simulation boxes contained one sulfur compound placed in the center of the box and 500 ion pairs for ILs or 500:1000 ChCl:HBD for DESs. All the systems were minimized using a steepest descent algorithm for 5000 steps to remove any poor contacts between molecules, followed by a 2 ns NPT equilibration step, and a 10 ns or 15 ns production step for the IL or DES systems, respectively.

Coordinates from the last snapshot of the production run were extracted and applied to the FEP-MD calculation, using an accurate and efficient leap-frog stochastic dynamics (*sd*) integrator.[67] The free energy change of transforming a system from state A (λ=0) to state B (λ=1), ΔG_{AB}, is a function of a coupling parameter, λ, which is applied to describe the level of change between states A and B. In this work, thirty-one λ windows have been used in the transformation (Table S7). To adjust the molecular interactions between solvent and sulfur compound along the changes of λ, the coulombic and van der Waals (vdW) interactions were coupled independently.[68] When the particles are close to appearing (λ close to 0 or 1), the interaction energy will be too weak to maintain the particle distance leading to singularities. In GROMACS[69] the "soft-core" potential (V_{sc}) was introduced to circumvent these problems and can be expressed using equations 5-7.[70]

$$V_{sc}(r) = (1-\lambda)V^A(r_A) + \lambda V^B(r_B) \tag{5}$$

$$r_A = (\alpha\, \sigma_A^6\, \lambda^P + r^6)^{\frac{1}{6}} \tag{6}$$

$$r_B = (\alpha\, \sigma_B^6\, (1-\lambda)^P + r^6)^{\frac{1}{6}} \tag{7}$$

The V^A and V^B are the van der Waals potentials in state A (λ=0, only solvent molecules) and state B (λ=1, one sulfur compound in the solvent box), α is the soft-core parameter, P is the soft-core λ power, and σ is the radius of the interaction. The values used for α, P, and σ were 0.5, 1.0, and 3.0 Å, respectively, as reported by Velarde-Salcedo *et al.*[65, 69] For each window (λ), the system was minimized using a steepest descent algorithm for 5000 steps, followed by a 2 ns NPT equilibration step and a 20 ns production step. The free energies were obtained through the BAR algorithm using the alchemical analysis program.[68]

Results and Discussion

Excess chemical potentials. Solvation free energies, ΔG_{solv}, describe the relative equilibrium populations of compounds in solution and gas phase and can provide insight into how solvent behaves in different environments.[71] The difference between the chemical potentials of component *i* in solution and gas phase ($\mu_{i,solv}$ - $\mu_{i,gas}$) is related to ΔG_{solv} in the thermodynamic limit of the solvated phase and the ideal gas limit of the gas phase. In the additional limit of one molecule of component *i* at infinite dilution, ΔG_{solv} becomes the infinite dilution excess chemical potential ($\mu_i^{ex,\infty}$) in the respective solvents.[71] Excess chemical potential values can be derived from infinite dilution activity coefficients (γ_i^∞) measurements using equation 8.[72]

$$\mu_i^{ex,\infty} = \Delta G_{solv}(T,P) = RT * (ln\gamma_i^\infty(T,P) + ln\frac{V_l(T,P)\, P_i^{sat}(T)}{RT}) \quad (8)$$

The V_l is the molar volume of solvent (m^3/mol), P_i^{sat} is the saturation vapor pressure (Pa), R is the molar gas constant Jmol^{-1}K^{-1} and T is temperature (K). Activity coefficients at infinite dilution, γ_i^∞, describe the thermodynamic nonideality between two substances that arise exclusively from solute-solvent intermolecular interactions, e.g., van der Waals and electrostatic interactions.[73] As such, γ_i^∞ and consequently $\mu_i^{ex,\infty}$ can be useful for vetting ILs and DESs as S-extractants if appropriate caution is taken.[74]

The $\mu_i^{ex,\infty}$ values were calculated here for the ILs/TS systems using FEP-MD simulations in conjunction with the 0.8*OPLS-2009IL and OPLS-VSIL force fields (Table 1 and Figure 1). Reported experimental measurements[75-81] and theoretical estimations[82] of γ_i^∞ (Table S5) were converted to $\mu_i^{ex,\infty}$ using equation 8 and provided for comparison (Table 1 and Figure 1). In the [BMIM][Cl]/TS system, the $\mu_i^{ex,\infty}$ computed using OPLS-VSIL FF was -4.298 ± 0.045 kcal/mol which was reasonably close to the experimental value -4.151 kcal/mol, whereas the 0.8*OPLS-2009IL FF gave a larger deviation with a value of -4.571 ± 0.061 kcal/mol. Calculations of the [BMIM]-IL/TS systems based on the [SCN], [BF_4], and [PF_6] anions also yielded $\mu_i^{ex,\infty}$ values comparable to experimental results with deviations of approximately 0.3-0.7 kcal/mol depending on the solvent or FF chosen (Table 1). In terms of excess free energy, the most favorable IL for the extractive desulfonation of thiophene at 298 K was [BMIM][NTf_2] from both the FEP-MD simulations and the theoretically derived $\mu_i^{ex,\infty}$ values. It should be noted that no experimental value of γ_i^∞ for [BMIM][NTf_2] was available at the time of publication. However, the γ_i^∞ of the [*sec*-BMIM][NTf_2] isomer has been reported[81] and yields a derived $\mu_i^{ex,\infty}$ value of -4.020 kcal/mol, which may be considered a reasonable estimate for [BMIM][NTf_2]. Overall, the computed $\mu_i^{ex,\infty}$ values of all the ILs systems studied here suggest that [BMIM][NTf_2] possesses the strongest potential as a desulfurization solvent extractant. FEP-MD/OPLS-VSIL simulations by Velarde-Salcedo *et al.*[65] also reported favorable $\mu_i^{ex,\infty}$ values for thiophene in [BMIM][BF_4] and [BMIM][CH_3COO] at higher temperatures of 300 and 343.15 K with the acetate-based IL possessing an additional advantage of a lower toxicity compared to fluorene-based ILs.[83]

Table 1. Calculated excess chemical potential, $\mu_i^{ex,\infty}$ (kcal/mol), for the IL-thiophene systems from FEP-MD simulations (0.8*OPLS-2009IL and OPLS-VSIL) and comparisons to $\mu_i^{ex,\infty}$ derived from theoretical and experimental infinite dilution activity coefficients, γ_i^∞, at 298 K.

IL	2009IL	VSIL	Theor.[a]	Exptl.[b]
[BMIM][Cl]	-4.571 ± 0.061	-4.298 ± 0.045	-3.866	-4.151
[BMIM][SCN]	-4.450 ± 0.047	-4.521 ± 0.044	-3.990	-4.116
[BMIM][BF_4]	-4.622 ± 0.069	-4.642 ± 0.056	-3.982	-3.944
[BMIM][PF_6]	-4.509 ± 0.093	-4.430 ± 0.069	-3.907	-4.054, -3.997
[BMIM][NTf_2]	-4.794 ± 0.068	-4.971 ± 0.053	-4.118	-

[a] Calculated from γ_i^∞ generated using the least-squares vector machine (LSSVM) method by Paduszyński.[82] [b] Calculated using experimentally reported γ_i^∞ values.[75-81]

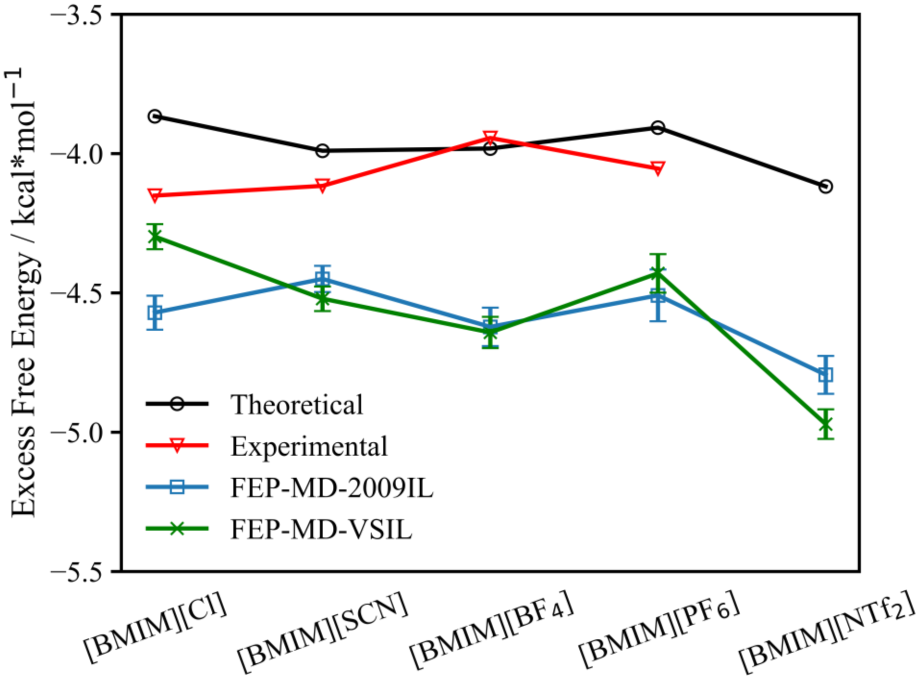

Figure 1. Comparison of excess chemical potential values for the IL/thiophene systems calculated using FEP-MD and derived from theoretical and experimental infinite dilution activity coefficients.

The $\mu_i^{ex,\infty}$ values were also calculated for DBT and MDBT in the 5 different ILs using FEP-MD simulations with both the 0.8*OPLS-2009IL and OPLS-VSIL FFs (Table 2 and Figure 2). At present, no experimental $\mu_i^{ex,\infty}$ energies are available for these refractory sulfur compounds in ILs so no direct comparisons can be made. However, similar to TS, the [BMIM][NTf_2] IL yielded the most favorable $\mu_i^{ex,\infty}$ energy for both the DBT and MDBT compounds at 298 K. Specifically, the simulations of [BMIM][NTf_2]/DBT gave comparable $\mu_i^{ex,\infty}$ values of -13.941 ± 0.154 and -13.962 ± 0.069 kcal/mol for 0.8*OPLS-2009IL and OPLS-VSIL FFs, respectively, and were approximately 0.4-1.2 kcal/mol more favorable than the other ILs (Table 2). The ILs/MDBT simulations predicted even lower $\mu_i^{ex,\infty}$ values compared to ILs/DBT, e.g., [BMIM][NTf_2]/MDBT energies of -15.197 ± 0.162 and -14.844 ± 0.087 kcal/mol using 0.8*OPLS-2009IL and OPLS-VSIL, respectively. Interestingly, the DBT and MDBT simulations revealed a trend correlating more favorable $\mu_i^{ex,\infty}$ energy to increasing IL anion size, with the exception of [BMIM][Cl] (Figure 2). The same observation was reported experimentally by Player *et al.*, where anion size influenced S-extraction efficiency of TS and DBT with a trend of [NTf_2] > [PF_6] > [BF_4] for [BMIM]-based ILs.[33] The same correlation between increasing IL anion volume and enhanced extraction efficiency has been reported elsewhere in the desulfurization and denitrogenation of fuel oils.[84, 85] This higher S-compound extraction efficiency has been hypothesized to arise from an increased surface area for absorption in the larger anions and, to a lesser extent, size-dependent changes in interaction energies between the IL ions themselves.[33]

Table 2. Calculated excess chemical potential, $\mu_i^{ex,\infty}$ (kcal/mol), for the IL-dibenzothiophene and IL-4-methyldibenzothiophene systems from FEP-MD simulations (0.8*OPLS-2009IL and OPLS-VSIL) at 298 K.

	DBT		**MDBT**	
	2009IL	**VSIL**	**2009IL**	**VSIL**
[BMIM][Cl]	-13.547 ± 0.041	-13.207 ± 0.172	-14.233 ± 0.249	-14.497 ± 0.119
[BMIM][SCN]	-12.788 ± 0.079	-12.787 ± 0.098	-13.262 ± 0.094	-13.326 ± 0.126
[BMIM][BF$_4$]	-13.228 ± 0.091	-13.305 ± 0.091	-14.057 ± 0.126	-13.876 ± 0.096
[BMIM][PF$_6$]	-13.555 ± 0.145	-13.553 ± 0.159	-14.489 ± 0.170	-13.934 ± 0.118
[BMIM][NTf$_2$]	-13.941 ± 0.154	-13.962 ± 0.069	-15.197 ± 0.162	-14.844 ± 0.087

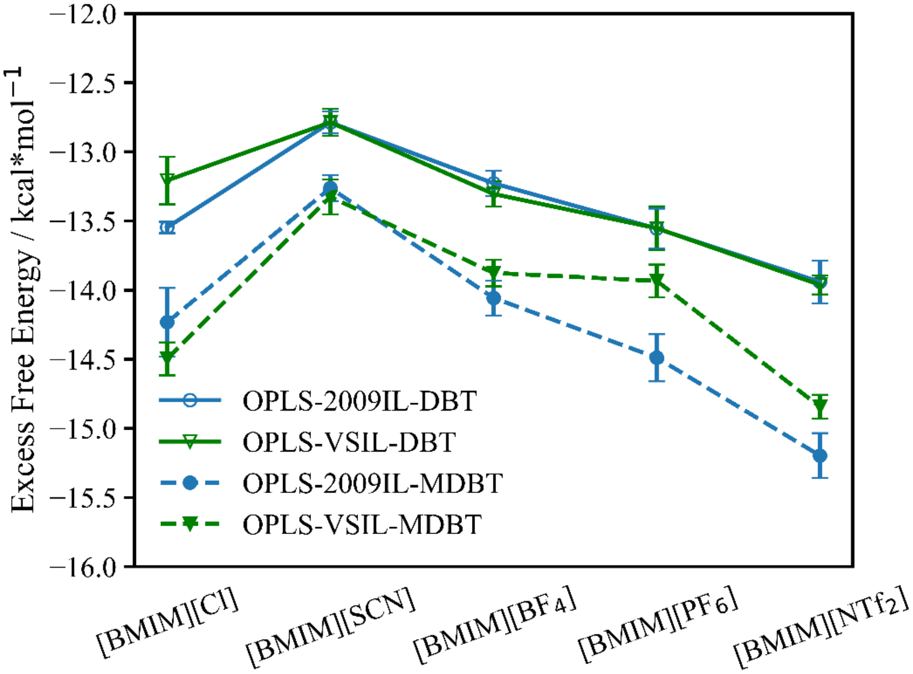

Figure 2. Calculated excess chemical potential values for ILs/DBT and ILs/MDBT systems using OPLS-based FFs.

Finally, $\mu_i^{ex,\infty}$ energies were computed for the 3 cyclic S-compounds in the CCEtg and CCGly DESs using FEP-MD/OPLS-DES (Table 3). The excess chemical potentials of TS, DBT, and MDBT were higher in energy by approximately 1-3 kcal/mol in the DESs than the ILs studied here (Tables 1-3). For example, the $\mu_i^{ex,\infty}$ for TS in CCEtg and CCGly were -3.601 ± 0.090 and -3.337 ± 0.090 kcal/mol, respectively, compared to values ranging from -4.2 to -5.0 kcal/mol in the different ILs. Accordingly, experimental examination of CCEtg by Li *et al.* found ~55% extraction efficiency of benzothiophene from *n*-octane,[38] whereas experiments by Rogošic and Kucan found an extraction efficiency of 5% to 35% for TS using 1:2 CCEtg from a model fuel composed of *n*-hexane, *n*-heptane, and *i*-octane.[86] In addition, practically no extraction of sulfur components was observed by Rogošic and Kucan when using CCEtg and real gasoline samples, which stresses that caution should be taken when utilizing model fuels for extraction studies.[86]

Table 3. Calculated excess chemical potential $\mu_i^{ex,\infty}$ (kcal/mol) for thiophene, dibenzothiophene, and 4-methyldibenzothiophene in deep eutectic solvents using FEP-MD simulations and the OPLS-DES FF at 298 K.

	CCEtg	**CCGly**
TS	-3.601 ± 0.090	-3.337 ± 0.090
DBT	-11.197 ± 0.191	-11.093 ± 0.108
MDBT	-11.607 ± 0.229	-11.618 ± 0.121

For a more comprehensive understanding of how the structure of ILs and DESs can influence the desulfurization of fuel, the intermolecular interactions between the cations, anions, HBDs, and cyclic sulfur compounds were investigated and analyzed in detail using unbiased MD simulations. Given that [BMIM][NTf$_2$] possessed the most favorable $\mu_i^{ex,\infty}$ values for TS, DBT, and MDBT, discussions here will primarily focus on this solvent. However, an equal and detailed analysis was performed for all ILs simulated, i.e., [BMIM][Cl], [BMIM][SCN], [BMIM][BF$_4$], and [BMIM][PF$_6$], and will be used for comparison (all data can be found in the supporting information). In terms of DESs, a detailed analysis of CCEtg is the provided in main text, whereas the same analysis of CCGly is available in the supporting information.

Thiophene/IL. The liquid structure between [BMIM], [NTf$_2$], and TS was analyzed using radial distribution functions (RDFs) which provides the average distribution of particles around a central reference particle (Table 4 and Figure 3). RDF plots of the [BMIM]-based [Cl], [SCN], [BF$_4$], and [PF$_6$] ILs are provided in the supporting information (Tables S8-S11 and Figures S1-S4). The two IL FFs utilized here, 0.8*OPLS-2009IL and OPLS-VSIL, gave similar *g(r)* intensities and atomic distances between the S-atom of TS, the H atoms of [BMIM], and the F and O atoms of the [NTf$_2$] anion. However, a notable difference in hydrogen bonding was found between the most acidic proton on the [BMIM] ring, i.e., H2-C2 bisecting the nitrogen atoms (Figure 3), and the S-atom from thiophene where the OPLS-VSIL yielded a closer interaction distance of 298.3 pm compared to 321.7 pm for 0.8*OPLS-2009IL. Intermolecular interactions involving the [BMIM]-H2 atom play a predominately large role in dictating solvent properties[87-89] and the OPLS-VSIL FF was fine-tuned during its creation to better reproduce this strong hydrogen bonding ability.[55] The [BMIM]-H2 proton also had a tighter atomic distance of 308.3 pm with TS in the [BMIM][PF$_6$] IL system from OPLS-VSIL compared to 335.0 pm for 0.8*OPLS-2009IL (Table S11). However, the remaining ILs had virtually no defining RDF peaks for the interactions between the TS and any of the H2/H4/H5 ring hydrogen atoms regardless of the FF utilized (Figures S1-S4). The larger volume anions [NTf$_2$] and [PF$_6$] allowed the [BMIM] cation to complex the imidazolium ring protons (H2/H4/H5) closer to the cyclic S-compound, perhaps as the result of a looser ion-ion liquid structure compared to the smaller anion ILs.[54, 55] The enhanced [BMIM]-thiophene intermolecular interactions relative to increasing anion size are consistent with the lower $\mu_i^{ex,\infty}$ energies and the greater S-compound extraction efficiencies measured experimentally.[33]

The RDF plots between the alkyl chain hydrogen atoms located adjacent to the imidazolium ring (H10 for methyl and H6 for butyl) and the S atom of TS gave large computed peak heights, e.g., *g(r)* values of 1.20-1.21 for H10-S and 1.04-1.15 for H6-S in [BMIM][NTf_2] (Table 4). Investigation of the *g(r)* values for the [Cl], [SCN], and [BF_4] ILs found H10-S and H6-S interactions that were generally below 1 and had ill-defined RDF peaks (Tables S8-S10). Instead, the largest *g(r)* peaks were between the H9 atom of [BMIM], which is on the terminal methyl group of the butyl sidechain, and the S atom of TS. For example, the *g(r)* of H9-S for [Cl], [SCN], [BF_4], [PF_6], and [NTf_2] was 1.35, 1.22, 1.18, 1.12, and 0.91, respectively, using OPLS-VSIL with similar values computed for 0.8*OPLS-2009IL (Tables 4 and S8-S11). A clear pattern between decreasing anion size and a preference for the TS molecule to occupy an area further away from the center of the imidazolium ring is evident. This may in part help explain the more favorable $\mu_i^{ex,\infty}$ values computed for [BMIM][NTf_2] (Table 1) given the importance of strong solute-solvent intermolecular interactions on excess chemical potentials.[73]

Another important conclusion from the RDF calculations is that TS had closer intermolecular distances and presumably stronger electrostatic/dispersion interactions with the IL anions rather than the cations. For example, MD simulations of [BMIM][NTf_2] found that the F and O atoms of [NTf_2] had RDF atomic distances of 271.7 and 265.0 pm, respectively, with H from TS. All other [BMIM]-ILs, i.e., [Cl], [SCN], [BF_4], and [PF_6], gave the same trend of a closer distance between the TS molecule and the anion, rather than with the cation (Tables S8-S11). Using [BMIM][Cl] as an example, the OPLS-VSIL computed RDFs between thiophene H-atoms and chloride gave the shortest distance of 278.3 pm and the highest *g(r)* intensity, 2.06, compared to any other interaction between TS and [BMIM] (Table S8). For comparison, *ab initio* MD (AIMD) simulations of [BMIM][Cl]/TS by Velarde-Salcedo *et al*. reported a comparable first peak intensity g(r) of 1.80 and a distance of 282 pm.[65] Similarly, for [BMIM][SCN] the N and S atoms of [SCN] had interaction distances of 255.0 and 268.3 pm with the H-atoms of TS, respectively, and large *g(r)* intensities of 1.24 and 1.39; the [BMIM] cation in this case was further away from TS, i.e., 321.7-335.0 pm, with smaller RDF peaks of 0.84-1.22 (Table S9). The [BMIM] [BF_4] and [BMIM][PF_6] ILs followed a similar pattern, but larger anions made the cation more competitive for interactions with TS (Tables S10 and S11). The present calculations agreed with previous classical MD and AIMD IL simulations that found stronger energetic interactions present between TS and anions compared to the cations.[65]

Table 4. Interaction distances (pm) and *g(r)* from radial distribution functions for the [BMIM][NTf$_2$]/TS system computed using molecular dynamics and the 0.8*OPLS-2009IL and OPLS-VSIL FFs.

	Distance		***g*(r)**	
Atoms[a]	**2009IL**	**VSIL**	**2009IL**	**VSIL**
H6-S	325.0	325.0[b]	1.15	1.04
H7-S	325.0	328.3	0.92	0.87
H8-S	328.3	328.3	0.96	0.84
H9-S	341.7	348.3[b]	1.02	0.91
H10-S	328.3	335.0	1.21	1.20
H2-S	321.7	298.3	1.04	1.09
H4,5-S	318.3	315.0	1.31	1.24
F-H	268.3	271.7	1.01	0.96
O-H	271.7	265.0	1.13	1.08

[a] Atom definitions provided in Figure 3. [b] The middle of the broad peak was chosen to represent the peak position.

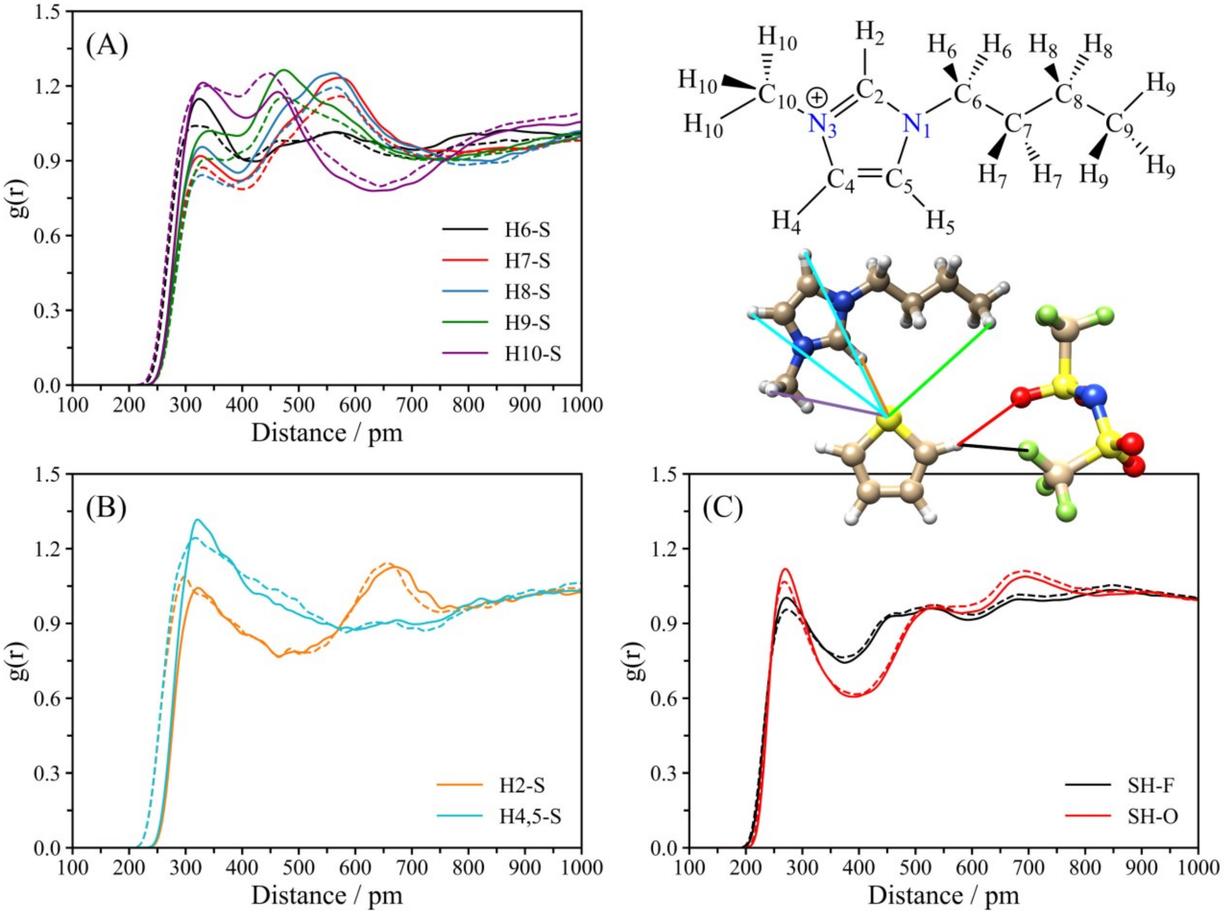

Figure 1. Computed radial distribution function plots between atoms in TS and [BMIM][NTf$_2$]. The solid lines correspond to the simulations using 0.8*OPLS-2009IL and the dashed lines refer to OPLS-VSIL. (A) Interactions between alkyl chain hydrogens of the [BMIM] cation and sulfur atom of TS. (B) Interactions between ring hydrogens of the [BMIM] cation and sulfur atom of TS. (C) Interactions between hydrogens of TS and fluorine/oxygen atoms of the [NTf$_2$] anion.

To further investigate important solute-solvent interactions present between TS and the ILs, two different types of combined distribution functions (CDFs) were calculated for the [BMIM][NTf$_2$]/TS system (Figure 4). The first CDF analyzed the potential for π-π stacking between TS and [BMIM] using the centers-of-rings (CoR) distance, $d_{\text{CoR-CoR+}}$, and the angle, α, formed between a normalized vector (RN) perpendicular to the plane of thiophene. The second CDF illustrated the relationship between two distances, the CoR of TS to the anion center-of-mass ($d_{\text{CoR-CoM}}$) and the $d_{\text{CoR-CoR+}}$ between TS and [BMIM]. Using this second CDF to examine any potential correlation between $d_{\text{CoR-CoR+}}$ and $d_{\text{CoR-CoM}}$ in [BMIM][NTf$_2$]/TS found a high interaction probability region between [BMIM] and TS that was near a $d_{\text{CoR-CoR+}}$ value of ~450 pm with a second interaction occurring around a second solvation shell distance of ~1000 pm. The TS-[NTf$_2$] interaction was localized around a $d_{\text{CoR-CoM}}$ of 650 pm (Figure 4 lower). Examination of the other four ILs found a similar pattern of $d_{\text{CoR-CoR+}}$ centralized around 500-550 pm with the optimal $d_{\text{CoR-CoM}}$ occurrence dependent on the size of the anion, e.g., around 500 pm for the smallest anions ([Cl] and [SCN]) and closer to 600 pm for the largest ([BF$_4$] and [PF$_6$]) (Figures S5-S8). Analysis of π-π stacking between TS and [BMIM] using the CDF that coupled $d_{\text{CoR-CoR+}}$ to α confirmed the highest probability of occurrence to be centered around 450 pm, but with specific angles of 0-15° or 175-180° (Figure 4 upper). For comparison, a typical equilibrium $d_{\text{CoR+-CoR+}}$ for two [BMIM] rings in pure IL has been reported to be approximately 400 pm.[55, 90] This suggests a preference for a slipped-parallel π-π stacking orientation between TS and the IL cation in [BMIM][NTf$_2$]/TS. Interestingly, π-π stacking between imidazolium cations in ILs has been shown to be influenced by the size of the anion with π-π stacking stabilized by smaller [Cl] or [NO$_3$] anions,[91] whereas weakly coordinating anions such as [BF$_4$] leads to an alternating cation-anion conformation.[92] However, a significant π-π stacking preference between TS and [BMIM] was found here regardless of the anion present in the system (Figures S5-S8) confirming the importance of this physical property to IL extraction ability.[51, 93]

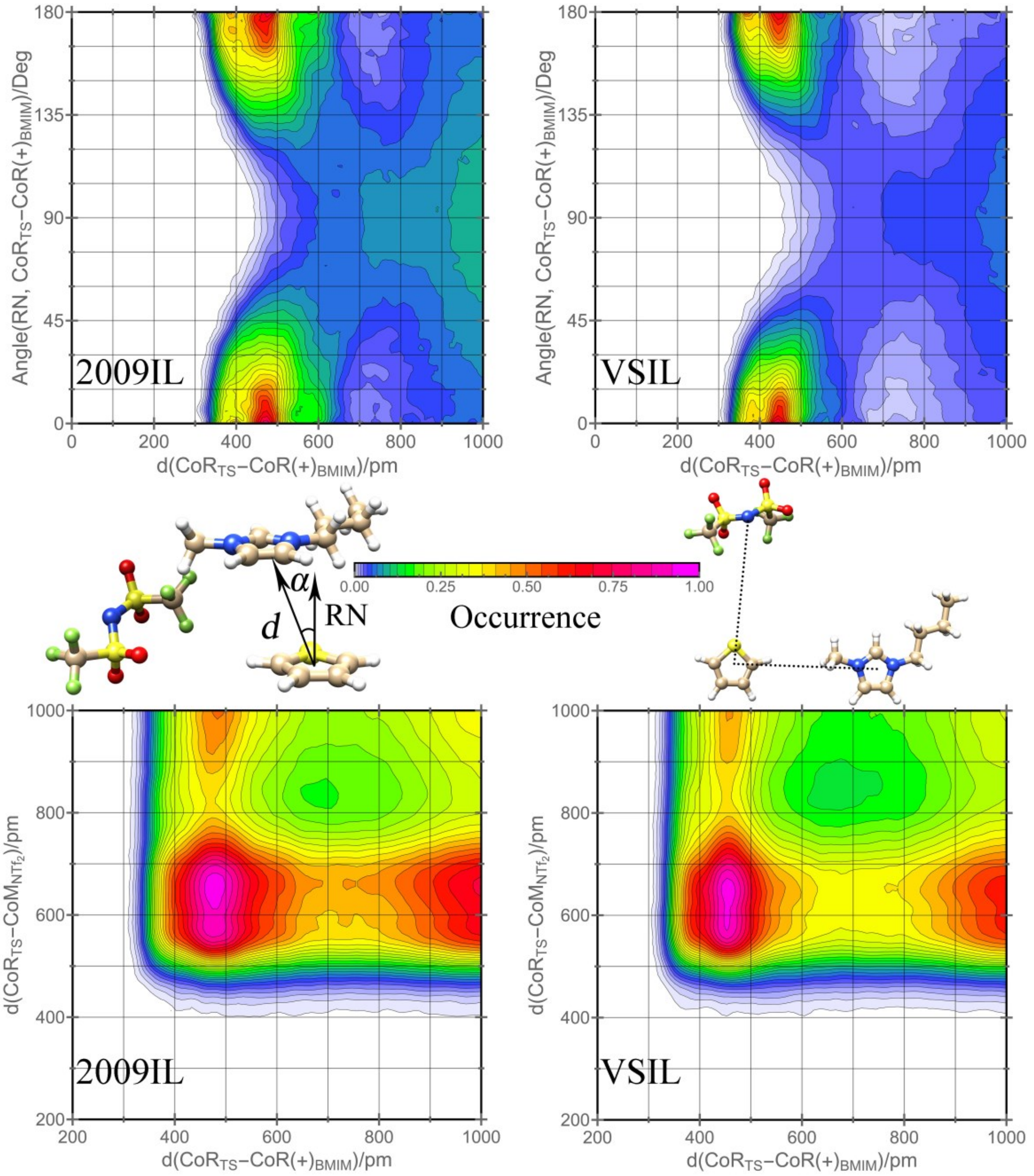

Figure 4. Combined distribution function (CDF) plots for [BMIM][NTf$_2$]/thiophene using the 0.8*OPLS-2009IL and OPLS-VSIL MD simulations. The upper two CDFs represent center-of-ring (CoR) interactions between [BMIM] cation and TS with the plotted angle *α* vs the distance *d*. The lower two CDFs represent two distances involving of CoR of TS and center-of-mass (CoM) of the [NTf$_2$] anion and the CoR-CoR(+) of TS and [BMIM]. Colors represent the frequency of interaction occurrence.

Spatial distribution functions (SDFs) were calculated to gain further insight into the population of favored ion positions around the thiophene molecule over the course of the simulation trajectory (Figure 5). The SDFs were built and analyzed using the TRAVIS program[63, 64] and the corresponding isosurface values for the different ions are provided in Table S12. Not surprisingly, the SDFs found that the [BMIM] cation preferred to occupy the area parallel to the face of the TS molecule indicative of the π-π stacking preference shown in the CDF analysis. Consequently, the anions were evenly distributed near the H-atoms of TS for the smaller ions, e.g., [Cl], [SCN], and $[BF_4]$, but the larger size of $[NTf_2]$ meant it was found primarily near the H-atoms located in in the lower region of TS, that is, away from the S-atom where the RDF calculations indicated a preference for a tighter [BMIM]-H2 and S-atom interaction (Table 4 and Figure 3).

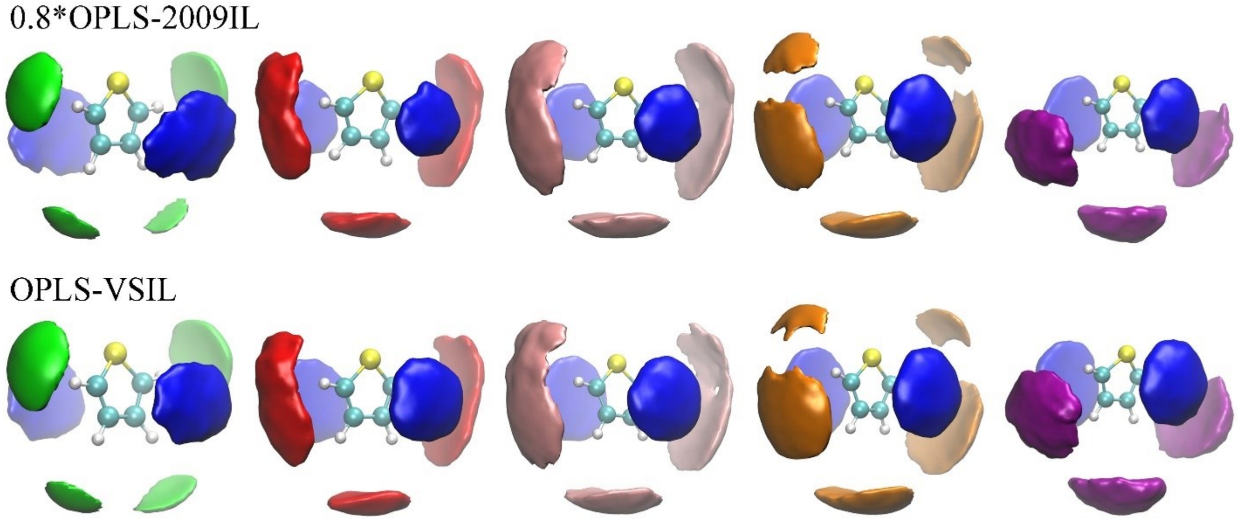

0.8*OPLS-2009IL

OPLS-VSIL

Figure 5. Spatial distribution functions (SDFs) of the [Cl] anion (green color), [SCN] anion (red color), $[BF_4]$ anion (pink color), $[PF_6]$ anion (orange color), $[NTf_2]$ anion (purple color), and [BMIM] cation (blue color) around the thiophene molecule (ball-and-stick) from MD simulations.

Finally, the average coordination number (N_{coord}) was obtained by dividing the MD trajectory into four equal parts and integrating the corresponding RDFs under the first peak (r_{max} or 1st solvation shell) to the first minimum (r_{min}) using the centers-of-masses between the cations, anions, and TS particles. Figure S9 provides the center-of-mass RDFs peak positions, heights, and shapes for [BMIM][NTf$_2$]/TS with the data for the other IL/TS systems given in Figures S10-S13. Unsurprisingly, the center-of-mass RDF between [BMIM] and [NTf$_2$] yielded the largest *g(r)* peak of around 2.3 and a close r_{max} distance of 508-520 pm (Table 5 and Figure S9). Despite the strong attraction between the oppositely charged ions, the r_{max} distance between [BMIM] and TS was shorter at 441-454 pm with 1.37-1.48 cations coordinated around thiophene (Table 5). Examination of the remaining [BMIM]-IL systems using OPLS-VSIL found similar complexation between [BMIM] and TS with a r_{max} distance of approximately 434-459 pm and a N_{coord} of 1.59, 1.59, 1.69, and 1.40 cations for the [Cl], [SCN], [BF$_4$], and [PF$_6$] systems, respectively (Tables S13-S16). While the number of cations interacting with TS appeared generally insensitive to the IL systems examined, the N_{coord} between the anions and TS did show a trend of increased N_{coord} with increasing anion size, for example, 3.6, 4.1, 4.5, 4.7, and 5.8 anions in the [Cl], [SCN], [BF$_4$], [PF$_6$], and [NTf$_2$] systems using OPLS-VSIL. The N_{coord} once again emphasized the importance of these strong anion-TS energetic interactions on S-compound extraction in ionic liquids.[65]

Table 5. Average coordination number (N_{coord}) and positions (pm) of the first maximum and first minimum in the center-of-mass RDFs between different particles in [BMIM][NTf$_2$]/TS.[a]

		0.8*OPLS-2009IL			OPLS-VSIL		
Center	**Shell**	$\mathbf{r_{max}}$	$\mathbf{r_{min}}$	$\mathbf{N_{coord}}$	$\mathbf{r_{max}}$	$\mathbf{r_{min}}$	$\mathbf{N_{coord}}$
[BMIM]	[BMIM]	880[b]	1324	19.9 ± 0.6	869[b]	1271	17.7 ± 0.4
[BMIM]	[NTf$_2$]	520	913	6.9 ± 0.1	508	889	6.3 ± 0.1
[NTf$_2$]	[NTf$_2$]	779	1270	17.5 ± 0.2	771	1256	16.9 ± 0.2
TS	[BMIM]	454	560	1.37 ± 0.13	441	564	1.48 ± 0.10
TS	[NTf$_2$]	650	828	5.4 ± 0.3	638	844	5.8 ± 0.2

[a]Center-of-mass RDFs plot provided in Figure S9. [b]The middle of the broad peak was applied to represent the peak position.

Dibenzothiophene/IL. Intermolecular interactions were investigated for dibenzothiophene (DBT) in a similar fashion to TS through the calculation of RDF plots. Accordingly, the *g(r)* intensities and atomic distances between the [BMIM][NTf$_2$] ions and DBT are given in Table 6 and Figure 6, whereas data for the other IL/DBT systems ([BMIM] paired with [Cl], [SCN], [BF$_4$], or [PF$_6$]) are provided in Figures S14-S17 and Tables S17-S20. The specific interaction between the most acidic ring proton, [BMIM]-H2, and the S-atom of DBT yielded a trend of increasing *g(r)* with increasing anion size, e.g., 0.69, 0.88, 1.07, 1.14, and 1.66 for [Cl], [SCN], [BF$_4$], [PF$_6$], and [NTf$_2$], respectively, using OPLS-VSIL (0.8*OPLS-2009IL yielded the same correlation). In addition, the systems possessing larger anions, e.g., [BMIM][PF$_6$] and [BMIM][NTf$_2$], had closer atomic H2-S distances of 348-361 pm compared to those with smaller anions, such as [BMIM][Cl] and [BMIM][SCN], which had longer lengths of 365-398 pm. The H4 and H5 aromatic hydrogens in [BMIM] had a larger atomic separation of 371.7 pm from the S atom of DBT in [BMIM][NTf$_2$] compared to H2, but still gave the second largest *g(r)* intensity of 1.27-1.30 using both FFs (Table

6). Given its proximity to the H2-atom, unsurprisingly the DBT-S and H6-butyl interaction in [BMIM][NTf_2] had the next highest *g(r)* intensity of 1.15-1.18 (Figure 6A), whereas the remaining alkyl-based H atoms had *g(r)* values less than 1 at same general distance range of ~328-348 pm (Figure 6A). Interestingly, the remaining DBT/IL systems gave reduced H4/H5-S *g(r)* intensities of 0.64-1.00 that were more comparable in intensity to the alkyl chain H6/H7/H8/H9/H10-S *g(r)* values of <1. In addition, the alkyl H-atoms had closer atomic distances of ~315-335 pm to DBT whereas the H4/H5 had more elongated distances of ~360-380 pm (Tables S17-S20 and Figures S14-S17). Alkyl chain length has been correlated with greater experimental extraction of DBT from dodecane; for example, a hexyl, butyl, and ethyl group on 1-alkyl-3-methylimidazolum-[BF_4] ILs gave 53.5%, 38.0%, and 17.0% desulfurization efficiency.[94] However, more recent efforts have suggested that alternative physiochemical solvent properties, e.g., anion effect and π-π stacking, play a bigger role in desulfurization than the alkyl chain moiety.[33, 93]

Examination of the solute-anion interactions, i.e., DBT-[NTf_2], found well-defined 1st solvation shell peaks from the RDF plots with slightly larger *g(r)* intensities for SH-O compared to SH-F (Figure 6C/D). Despite the larger size of DBT, the atomic distance separation between SH-F and SH-O fell within ranges of 268.3-278.3 pm and 268.3-271.7 pm, respectively, which were comparable in magnitude to the smaller TS solute in [BMIM][NTf_2] (Tables 4 and 6). The DBT systems also featured the same pattern as TS where larger IL anions, i.e., [NTf_2] and [PF_6], made [BMIM] more competitive for favorable interactions with the solute. However, all anions ([Cl], [SCN], [BF_4], [PF_6], and [NTf_2]) still yielded closer and presumably stronger nonbonded interactions with DBT than the cations overall (Tables 6 and S17-S20). DFT calculations have suggested dispersion-driven binding between thiophene and IL ions with a positive correlation found between larger anion sizes and greater experimental S-extraction efficiency.[33]

Table 6. Interaction distances (pm) and *g(r)* from radial distribution functions for the [BMIM][NTf_2]/DBT system computed using molecular dynamics and the 0.8*OPLS-2009IL and OPLS-VSIL FFs.

	Distance		***g*(r)**	
Atoms[a]	**2009IL**	**VSIL**	**2009IL**	**VSIL**
H6-S	348.3	338.3[b]	1.15	1.18
H7-S	325.0	328.3	0.80	0.76
H8-S	318.3	328.3	0.77	0.63
H9-S	331.7	348.3	0.84	0.69
H10-S	-[c]	-[c]	-[c]	-[c]
H2-S	351.7	348.3	1.56	1.66
H4,5-S	371.7	371.7	1.30	1.27
SH1-F	271.7	271.7	0.97	0.89
SH2,3-F	275.0	278.3	1.05	0.97
SH4-F	271.7	268.3	0.91	0.85
SH1-O	268.3	271.7	1.06	1.01
SH2,3-O	271.7	271.7	1.11	0.97
SH4-O	268.3	268.3	1.23	1.17

[a]Atom definitions provided in Figure 6. [b]The middle of the broad peak was chosen to represent the peak position. [c]No well-defined peak available.

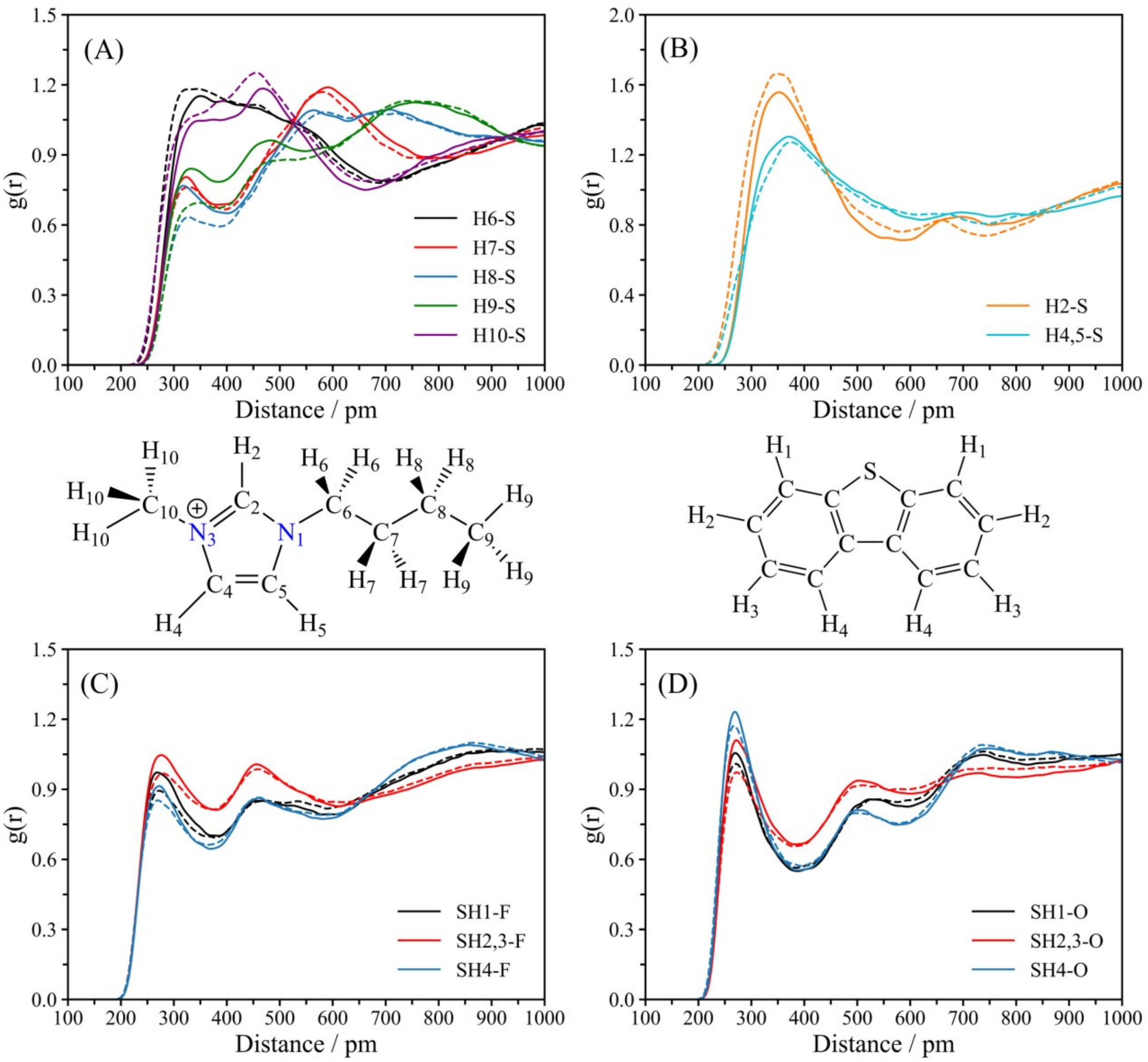

Figure 6. Computed radial distribution function plots between atoms in DBT and [BMIM][NTf$_2$]. The solid lines correspond to the simulations using 0.8*OPLS-2009IL and the dashed lines refer to OPLS-VSIL. (A) Interactions between alkyl chain hydrogens of the [BMIM] cation and sulfur atom of DBT. (B) Interactions between ring hydrogens of the [BMIM] cation and sulfur atom of DBT. (C) and (D) Interactions between hydrogens of DBT and fluorine/oxygen atoms of the [NTf$_2$] anion.

Two types of CDFs were computed for the IL/DBT systems featuring plots of (1) $d_{\text{CoR-CoR+}}$ versus α to examine π-π stacking potential and (2) $d_{\text{CoR-CoR+}}$ versus $d_{\text{CoR-CoM}}$ to investigate any correlation between cation-DBT and anion-DBT interactions (Figures 7 and S18-S21). Both FFs found the majority of [BMIM] cations to be located within a distance range of 360-390 pm from DBT with preferred angles α = 0°-15° or 165°-180° representing an idealized π-π sandwich assembly. The $d_{\text{CoR-CoR+}}$ versus $d_{\text{CoR-CoM}}$ CDF plots in [BMIM][NTf_2] showed a high occurrence of [BMIM]-DBT interactions localized at the same 360-390 pm distance with a [NTf_2]-DBT interaction range of 640-790 pm for OPLS-VSIL (or 650-810 pm for 0.8*OPLS-2009IL). This $d_{\text{CoR-CoR+}}$ for [BMIM]-DBT was tighter than the longer ~440-500 pm distance computed for [BMIM]-TS. Overall, the liquid structure appeared to be more ordered for [BMIM][NTf_2]/DBT than that of [BMIM][NTf_2]/TS (Figure 4). The smaller anion systems ([Cl] and [SCN]) also showed highly ordered π-π stacking but featured a looser anion-DBT structure compared to [BMIM][NTf_2]. For example, the [BMIM][Cl]/DBT system (Figure S18) included significant parallel π-π stacking between the [BMIM] and DBT with an α = 0-10°, but an extremely wide range of distances for DBT and chloride interaction occurrences. As the anion volume increases from [SCN] to [BF_4] to [PF_6], the highly ordered π-π stacking between [BMIM] and DBT is maintained, but the DBT-anion interactions become more localized and structurally ordered (Figures S19-S21). Accordingly, SDF analysis of all the [BMIM]-IL systems found highly consistent parallel π-π stacking between [BMIM] and DBT (blue color in Figure 8) and the IL anions distributed evenly around the DBT hydrogen atoms.

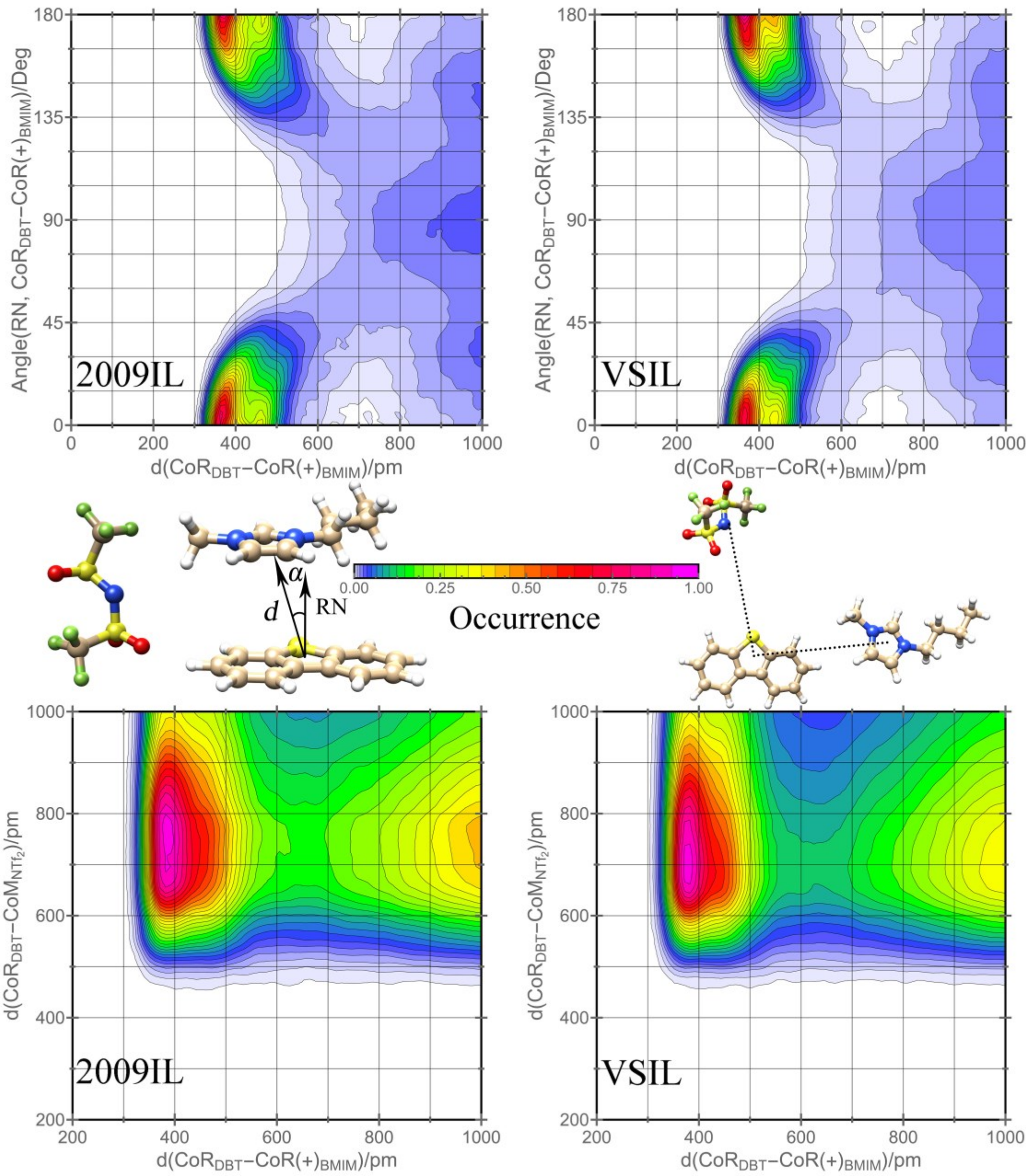

Figure 7. Combined distribution function (CDF) plots for [BMIM][NTf$_2$]/dibenzothiophene using the 0.8*OPLS-2009IL and OPLS-VSIL MD simulations. The upper two CDFs represent center-of-ring (CoR) interactions between [BMIM] cation and DBT with the plotted angle *α* vs the distance *d*. The lower two CDFs represent two distances involving of CoR of DBT and center-of-mass (CoM) of the [NTf$_2$] anion and the CoR-CoR(+) of DBT and [BMIM]. Colors represent the frequency of interaction occurrence.

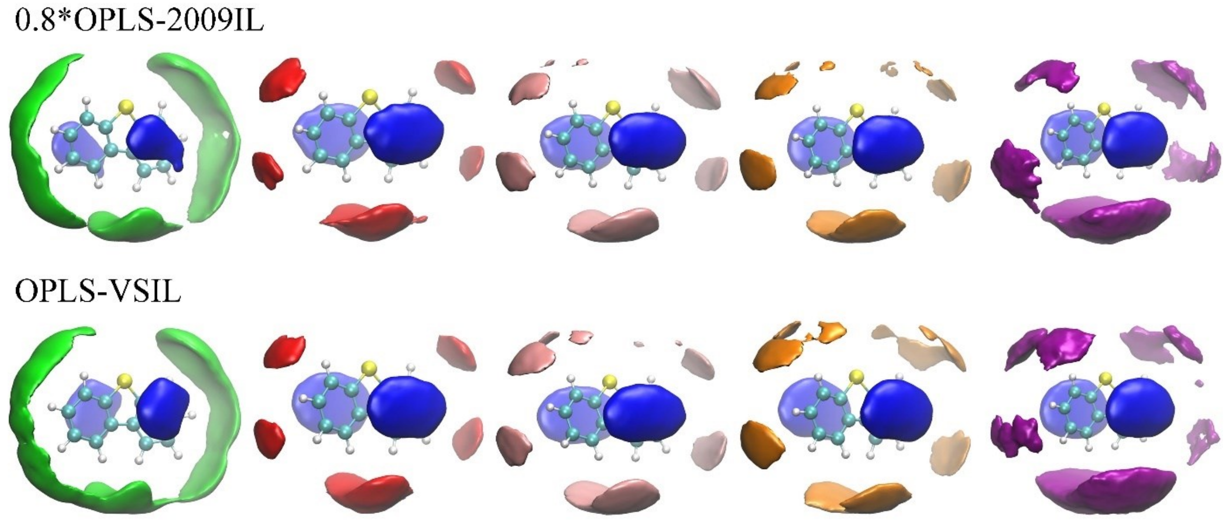

Figure 8. Spatial distribution functions (SDFs) of the [Cl] anion (green color), [SCN] anion (red color), [BF$_4$] anion (pink color), [PF$_6$] anion (orange color), [NTf$_2$] anion (purple color), and [BMIM] cation (blue color) around dibenzothiophene (ball-and-stick) from MD simulations.

The average coordination numbers (N_{coord}) for [BMIM][NTf$_2$]/DBT was computed by integrating under the first peak of the center-of-mass RDF plots given in Figure S22. Reasonable agreement was found between both FF predictions with the exception that shorter ion-DBT first maximum peaks (r_{max}) were computed using OPLS-VSIL compared to 0.8*OPLS-2009IL, e.g., DBT-[NTf$_2$] r_{max} values of 696 and 749 pm, respectively (Table 7). However, both FFs gave similar N_{coord} values of ~10 [NTf$_2$] anions and ~2 [BMIM] cations coordinated around DBT. From the SDF plots, it is evident that the two [BMIM] cations complex to the face of DBT in a parallel π-π stacking orientation and the anions surround the edges of the refractory sulfur compound (Figure 8). The coordination number of ~10 [NTf$_2$] to a single DBT was nearly double of that of 5.4-5.8 anions for TS (Table 5). This observation is best explained by the greater amount of surface area in DBT available for anion complexation as opposed to more favorable electrostatics/dispersion than TS-[NTf$_2$]. The center-of-mass RDF plots, $r_{\max}$, $r_{\min}$, and N_{coord} for the [BMIM][Cl], [BMIM][SCN], [BMIM][BF$_4$], and [BMIM][PF$_6$] ILs with DBT are provided in Figures S23-S26 and Tables S22-S25.

Table 7. Average coordination number (N_{coord}) and positions (pm) of the first maximum and first minimum in the center-of-mass RDFs between different particles in [BMIM][NTf$_2$]/DBT.[a]

		0.8*OPLS-2009IL			**OPLS-VSIL**		
Center	**Shell**	**$r_{\max}$**	**$r_{\min}$**	**N_{coord}**	**$r_{\max}$**	**$r_{\min}$**	**N_{coord}**
[BMIM]	[BMIM]	881[b]	1309	19.2 ± 0.2	864[b]	1250	16.8 ± 0.6
[BMIM]	[NTf$_2$]	520	901	6.7 ± 0.1	504	888	6.3 ± 0.1
[NTf$_2$]	[NTf$_2$]	776	1285	18.0 ± 0.1	785	1260	16.9 ± 0.2
DBT	[BMIM]	435	613	1.99 ± 0.14	420	588	1.87 ± 0.05
DBT	[NTf$_2$]	749	1061	10.7 ± 0.2	696	1045	10.1 ± 0.3

[a]Center-of-mass RDFs plot provided in Figure S22. [b]The middle of the broad peak was applied to represent the peak position.

4-Methyldibenzothiophene/IL. The final refractory sulfur compound system studied in ionic liquids was 4-methyldibenzothiophene (MDBT). Given the structural similarity between TS, DBT, and MDBT (Scheme 1), it was not surprising that the RDF plots for MDBT in [BMIM][NTf$_2$] followed similar trends to the other S-compounds, e.g., H2-S had the highest *g(r)* intensity followed by the 2nd and 3rd largest *g(r)* peaks for the butyl proton H6-S and the ring protons H4/H5-S (Table 8 and Figure 9). In addition, the H2-S *g(r)* intensities in the different [BMIM]-ILs were dependent upon increasing anion size, i.e., 0.67, 0.93, 1.09, 1.17, and 1.59 for [Cl], [SCN], [BF$_4$], [PF$_6$], and [NTf$_2$], respectively, from 0.8*OPLS-2009IL (with an identical pattern found using OPLS-VSIL) (Tables S26-S29 and Figures S27-S30). Other similarities in S-compound solvation were noted such as weaker interactions with the alkyl-based H7/H8/H9/H10 atoms (*g(r)* < 1) and closer atomic distances between MDBT and [NTf_2] (~265-281 pm) compared to MDBT and [BMIM] (~328-378 pm) (Table 8). One notable difference was a slightly weaker interaction between the H4/H5 ring protons and MDBT as compared to TS and DBT. For example, the *g(r)* intensity for H4/H5-S was reduced to 1.19 for MDBT compared to 1.27 for DBT and 1.24 for TS in the [BMIM][NTf_2] (from OPLS-VSIL in Tables 6 and 4). This distinction is likely derived from an increased steric hindrance between the methyl group of MDBT and the cation.

Table 8. Interaction distances (pm) and *g(r)* from radial distribution functions for the [BMIM][NTf$_2$]/MDBT system computed using molecular dynamics and the 0.8*OPLS-2009IL and OPLS-VSIL FFs.

	Distance		**g(r)**	
Atoms[a]	**2009IL**	**VSIL**	**2009IL**	**VSIL**
H6-S	348.3	328.3	1.18	1.21
H7-S	331.7	328.3	0.66	0.76
H8-S	318.3	331.7	0.63	0.61
H9-S	335.0	338.3	0.68	0.67
H10-S	338.3	-[b]	1.01	-[b]
H2-S	341.7	351.7	1.59	1.69
H4,5-S	371.7	378.3	1.18	1.19
SH1-F	271.7	278.3	0.99	0.86
SH2,3-F	281.7	281.7	1.01	0.95
SH4,5-F	271.7	271.7	0.93	0.84
SH6,7-F	271.7	275.0	0.94	0.89
SH8-F	281.7	288.3	0.87	0.80
SH1-O	268.3	268.3	1.14	0.99
SH2,3-O	271.7	271.7	1.11	0.97
SH4,5-O	268.3	265.0	1.20	1.13
SH6,7-O	275.0	271.7	1.05	0.93
SH8-O	281.7	281.7	0.86	0.80

[a] Atom definitions provided in Figure 9. [b] No well-defined peak available.

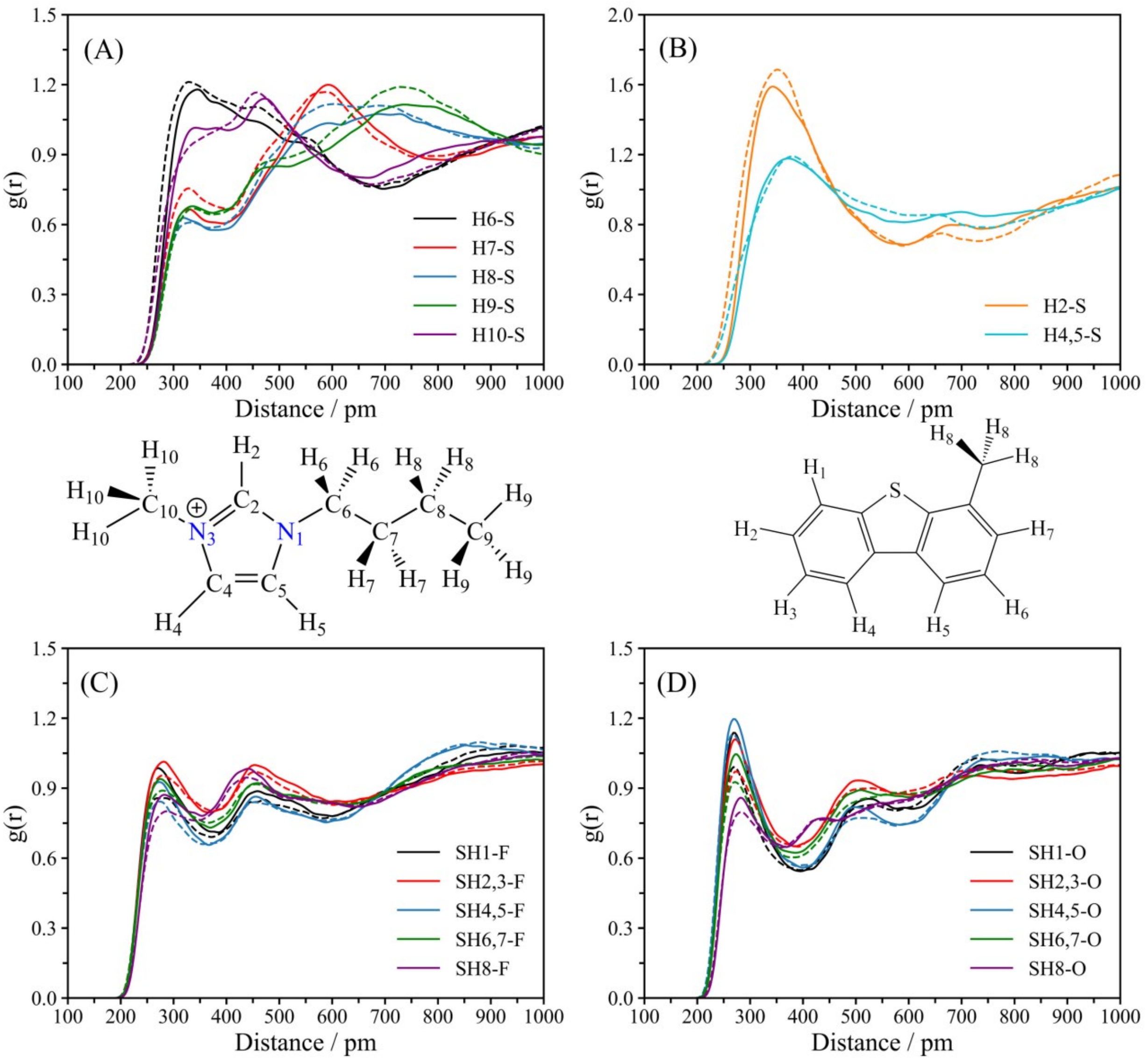

Figure 9. Computed radial distribution function plots between atoms in MDBT and [BMIM][NTf$_2$]. The solid lines correspond to the simulations using 0.8*OPLS-2009IL and the dashed lines refer to OPLS-VSIL. (A) Interactions between alkyl chain hydrogens of the [BMIM] cation and sulfur atom of MDBT. (B) Interactions between ring hydrogens of the [BMIM] cation and sulfur atom of MDBT. (C) and (D) Interactions between hydrogens of MDBT and fluorine/oxygen atoms of the [NTf$_2$] anion.

Examination of the intermolecular interactions between MDBT and the [BMIM] cation using CDFs emphasized a parallel π-π stacking with a $d_{\mathrm{CoR\text{-}CoR+}}$ of 360-380 pm using OPLS-VSIL (or 380-400 pm with 0.8*OPLS-2009IL) and α values near 0° and 180° (Figure 10). Simulations of the remaining ILs [BMIM][Cl], [BMIM][SCN], [BMIM][BF_4], and [BMIM][PF_6] also predicted an idealized π-π sandwich assembly between MDBT and the cation (Figures S31-S34). The $d_{\mathrm{CoR\text{-}CoM}}$ CDF for [BMIM][NTf_2] showed the largest probability of [BMIM]-MDBT interaction occurrences at distances of ~700-800 pm with a similar liquid structure compared to the [BMIM][NTf_2]/DBT solution (Figures 7 and 10). The IL systems with smaller anions, [Cl] and [SCN], showed significant disorder between the solute and the anions, whereas the particles in solutions became more ordered with the increasing anion size of [BF_4] and [PF_6] (Figures S31-S34). The computed SDFs for the IL/MDBT systems corroborated that the most probable location for [BMIM] was near the solute with π-π sandwich formation (blue color in Figure 11). The SDF analysis also found that the anions were localized near the MDBT H-atoms and occupied positions perpendicular to the solute ring. Interestingly, the substitution of the *ortho* position H1-atom in DBT with a methyl group in MDBT led to comparative differences in anion distribution near the *meta* hydrogens. For example, in [BMIM][NTf_2]/MDBT the SDF distribution area of H2 and H3 was sharply reduced for 0.8*OPLS-2009IL and largely disappeared for OPLS-VSIL compared to [BMIM][NTf_2]/DBT (Figures 8 and 11). The asymmetrical configuration of MDBT also impacted the SDF distribution of [BMIM] which preferred to occupy the location over the methylated benzene ring. All isosurface values for MDBT-based SDFs are provided in Table S30.

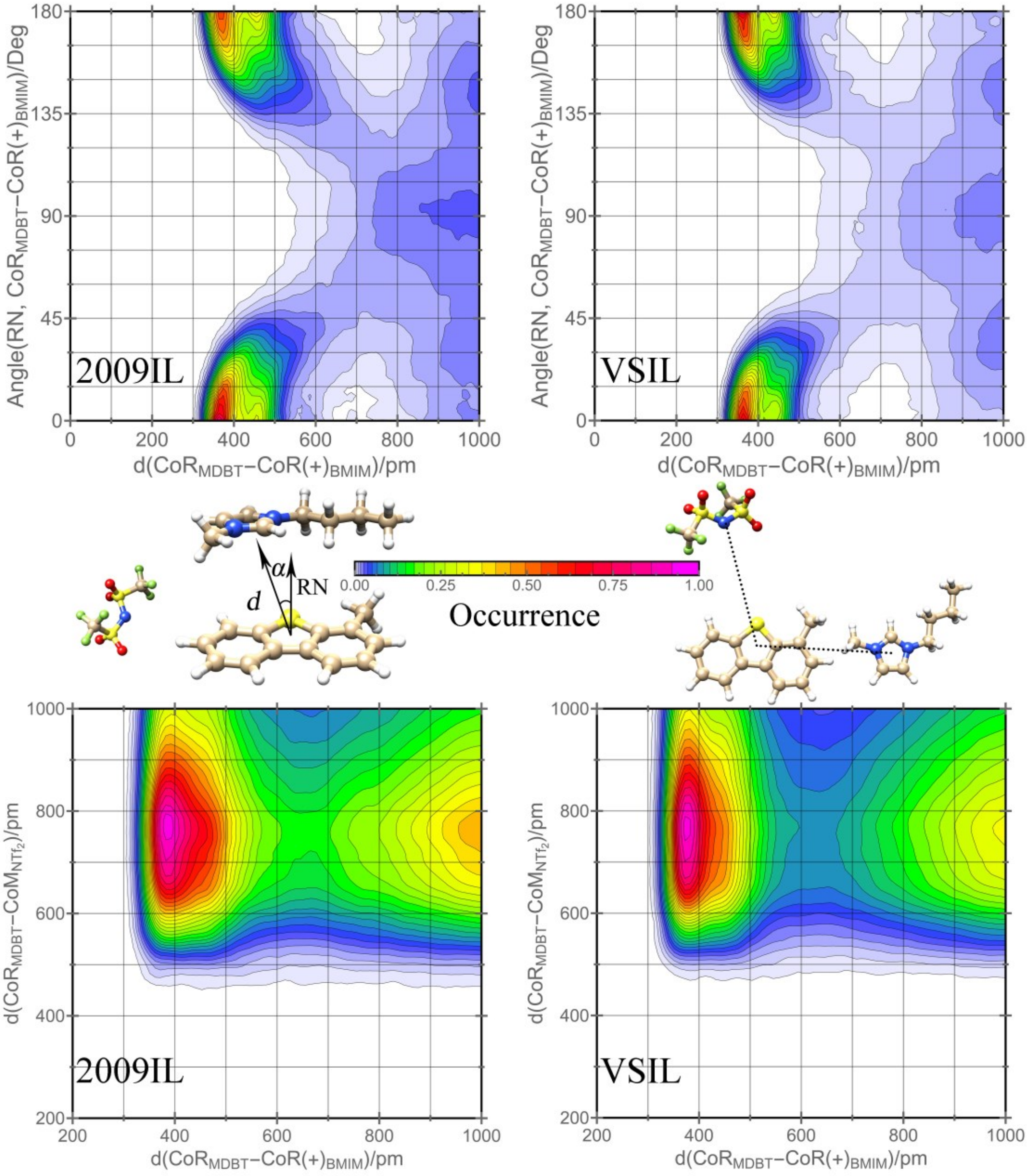

Figure 10. Combined distribution function (CDF) plots for [BMIM][NTf$_2$]/4-methyldibenzothiophene using the 0.8*OPLS-2009IL and OPLS-VSIL MD simulations. The upper two CDFs represent center-of-ring (CoR) interactions between [BMIM] cation and MDBT with the plotted angle *α* vs the distance *d*. The lower two CDFs represent two distances involving of CoR of MDBT and center-of-mass (CoM) of the [NTf$_2$] anion and the CoR-CoR(+) of MDBT and [BMIM]. Colors represent the frequency of interaction occurrence.

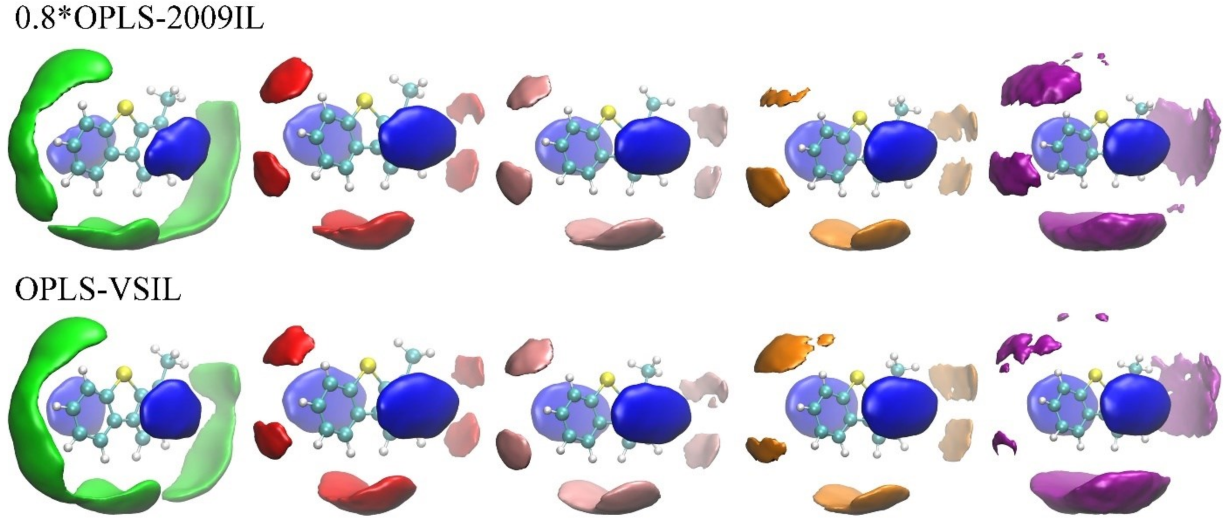

Figure 11. Spatial distribution functions (SDFs) of the [Cl] anion (green color), [SCN] anion (red color), [BF_4] anion (pink color), [PF_6] anion (orange color), [NTf_2] anion (purple color), and [BMIM] cation (blue color) around 4-methyldibenzothiophene (ball-and-stick) from MD simulations.

The average coordination numbers (N_{coord}) for [BMIM][NTf_2]/MDBT are provided in Table 9 and were computed by integrating under the first peak of the center-of-mass RDF plots given in Figure S35. The findings were relatively similar to DBT with N_{coord} values of ~10 [NTf_2] anions and ~2 [BMIM] cations coordinated around MDBT. The r_{max} peak for MDBT-[BMIM] and MDBT-[NTf_2] were located at 416 and 756 pm for OPLS-VSIL, respectively, and were close to the distances computed for the [BMIM][NTf_2]/DBT simulations (Tables 7 and 9). The center-of-mass RDFs and N_{coord} values for the remaining IL/MDBT systems can be found in the supporting information (Figures S36-S39 and Tables S31-S34).

Table 9. Average coordination number (N_{coord}) and positions (pm) of the first maximum and first minimum in the center-of-mass RDFs between different particles in [BMIM][NTf$_2$]/MDBT.[a]

		0.8*OPLS-2009IL			**OPLS-VSIL**		
Center	**Shell**	$\mathbf{r_{max}}$	$\mathbf{r_{min}}$	$\mathbf{N_{coord}}$	$\mathbf{r_{max}}$	$\mathbf{r_{min}}$	$\mathbf{N_{coord}}$
[BMIM]	[BMIM]	879[b]	1319	19.6 ± 0.5	869[b]	1268	17.5 ± 0.4
[BMIM]	[NTf$_2$]	520	921	7.0 ± 0.1	504	884	6.3 ± 0.1
[NTf$_2$]	[NTf$_2$]	773	1279	17.7 ± 0.1	769	1263	17.0 ± 0.3
MDBT	[BMIM]	435	616	1.96 ± 0.12	416	590	1.90 ± 0.08
MDBT	[NTf$_2$]	753	1036	9.9 ± 0.3	756	1060	10.6 ± 0.1

[a]Center-of-mass RDFs plot provided in Figure S35. [b]The middle of the broad peak was applied to represent the peak position.

Deep Eutectic Solvents. The excess chemical potential calculations carried out for the two DESs composed of choline chloride and ethylene glycol or glycerol, i.e., CCEtg and CCGly (Scheme 3), were less favorable by 1-3 kcal/mol compared to the ILs examined (Tables 1-3). Despite this finding, DESs still possess incredible potential as sulfur-compound extractants[39-41] and were investigated in detail here at the atomic level using MD simulations. RDF plots were first analyzed between the S-atom of the TS, DBT, and MDBT molecules and the two chemically unique hydrogen atom types (Hc and Ho) from Etg (Figure 12 and Table 10). The largest *g(r)* intensity computed was between the sulfur atom and the Hc atom located on the Etg methylene bridge with atomic separation distances of 318.3-321.7 pm. A trend was found where increasing the size of the S-compound led to a decrease in the first peak height for the Hc-S interaction, i.e., *g(r)* of 1.19, 0.98, and 0.83 for TS, DBT, and MDBT, respectively (Table 10). Conversely, the other unique Etg hydrogen atom type, i.e., Ho from the hydroxy groups, had little to no favorable interactions with the cyclic sulfur compounds as the Ho-S separation distance was >400 pm

(Figure 12). Instead, the Ho atoms interacted with the solvent chloride anions at significantly shorter Ho-Cl distances of 205.0-208.3 pm with extremely large *g(r)* intensities of 12.9-13.0 (Table S35 and Figure S40).

Examination of RDFs between TS/DBT/MDBT and the choline cations found overall weak interactions with *g(r)* intensities less than 1 for most hydrogen-sulfur interactions (Table 10). The first peak examined was between the S atom and the H1 atoms located on methyl groups attached to the N atom of choline (Figure 12). In this case, a minor dependence on solute size was noted, e.g., TS, DBT, and MDBT *g(r)* values of 0.96, 0.83, and 0.79 at distances of ~331-335 pm (Table 10). The next choline-solute interaction examined was between the H4 atom located on the choline hydroxyl group and the S atom from TS/DBT/MDBT that gave *g(r)* values of 0.90-0.93 with substantial H4-S separation distances of 378.3-391.7 pm. Rather than interacting with the solutes, the H4 atom formed strong hydrogen bonds with the solvent chloride anions as exemplified by the short H4-Cl distance of 218.3 pm and large *g(r)* intensities of 4.68-4.77 for all three cyclic sulfur molecules (Table S35). Finally, the interactions between the H2 and H3 atoms on choline and the S atom had separation distances between 308.3-328.3 pm depending on the solute and featured the smallest *g(r)* peak heights of 0.56-0.80. Given the generally weak interactions between the solvent components (Ch and Etg) and the TS/DBT/MDBT molecules, the results are consistent with the modest experimental extraction efficiencies of CCEtg when used to remove thiophene and benzothiophene from model fuels and gasoline.[38, 86] An inspection of the RDFs computed for the CCGly DES system with TS/DBT/MDBT yielded the same insight with overall smaller *g(r)* peaks present between choline/glycol and the sulfur compounds compared to the stronger electrostatic interactions and π-π interactions derived from the IL systems (Figure S41-S42 and Tables S36-S37).

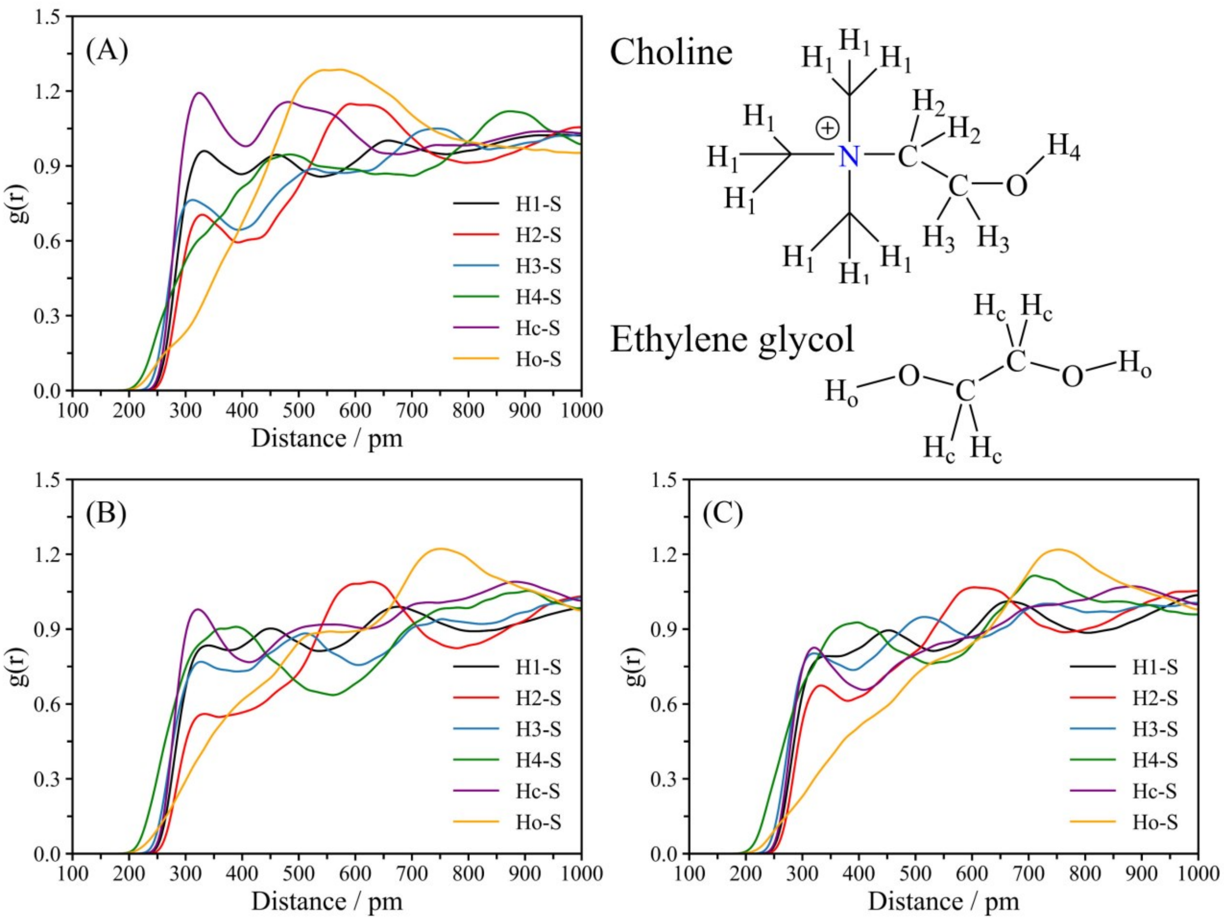

Figure 12. Computed radial distribution function plots between the sulfur atoms in (A) thiophene, (B) dibenzothiophene, and (C) 4-methyldibenzothiophene paired with hydrogen atoms from choline and ethylene glycol in the CCEtg DES.

Table 10. Interaction distances (pm) and *g(r)* from radial distribution functions in CCEtg between the S-atom in TS/DBT/MDBT and the H-atoms in choline and ethylene glycol.

	Distance (pm)			*g(r)*		
Atoms[a]	**TS**	**DBT**	**MDBT**	**TS**	**DBT**	**MDBT**
H1-S	331.7	335.0	335.0	0.96	0.83	0.79
H2-S	325.0	328.3	328.3	0.70	0.56	0.67
H3-S	308.3	318.3	315.0	0.76	0.76	0.80
H4-S	-[b]	378.3[c]	391.7[c]	-[b]	0.90	0.93
Hc-S	321.7	318.3	321.7	1.19	0.98	0.83
Ho-S	-[b]	-[b]	-[b]	-[b]	-[b]	-[b]

[a]Atom definitions provided in Figure 12. [b]No well-defined peak available between 300-400 pm. [c]The middle of the broad peak was chosen to represent the peak position.

Combined distribution function (CDF) plots of the distance between the solute center-of-ring and the chloride center-of-mass, *d*($\mathrm{CoR_{TS/DBT/MDBT}}$-$\mathrm{CoM_{Cl}}$), versus the distance between the solute center-of-ring and the choline center-of-mass, *d*($\mathrm{CoR_{TS/DBT/MDBT}}$-$\mathrm{CoM_{Ch}}$), were computed to examine any potential correlation between the solute-ions interactions in the CCEtg and CCGly DESs (Figures 13 and S43). The *d*($\mathrm{CoR_{TS}}$-$\mathrm{CoM_{Cl}}$) for the CCEtg/TS system indicated that the most intense interaction occurred between TS and $\mathrm{Cl^-}$ at approximately 500 pm with a second weaker intensity at ~700 pm (*y-axis* in Figure 13). The CCEtg/DBT and CCEtg/MDBT systems yielded the strongest intensities near the 720 pm region for the chloride-solute interaction, although significant probability of interaction existed over a large range of ~550-900 pm. As the *d*($\mathrm{CoR_{DBT/MDBT}}$-$\mathrm{CoM_{Cl}}$) distance is computed using the center-of-ring for the solutes it is expected for DBT/MDBT to have longer interacting distances with $\mathrm{Cl^-}$ compared to TS given their larger sizes. Overall, the $\mathrm{Cl^-}$ interaction distances appeared to be very fluid in all the DES systems studied, which may not be surprising given its stronger electrostatic interactions with the choline cation and the Etg and Gly hydrogen bond donors. Examining $d(\mathrm{CoR_{DBT/MDBT}}\text{-}\mathrm{CoM_{Ch}})$ found a considerably more localized interaction between the choline cation and the DBT/MDBT solutes with strong intensities computed primarily in the 440-460 pm region with a second solvation shell appearing at >1000 pm (*x-axis* in Figure 13). However, the $d(\mathrm{CoR_{TS}}\text{-}\mathrm{CoM_{Ch}})$ intensities suggested a significantly more fluid interaction, perhaps a consequence of the smaller size of TS, with a high probability of occurrence over a wide distance range of 420-700 pm at the first solvation shell.

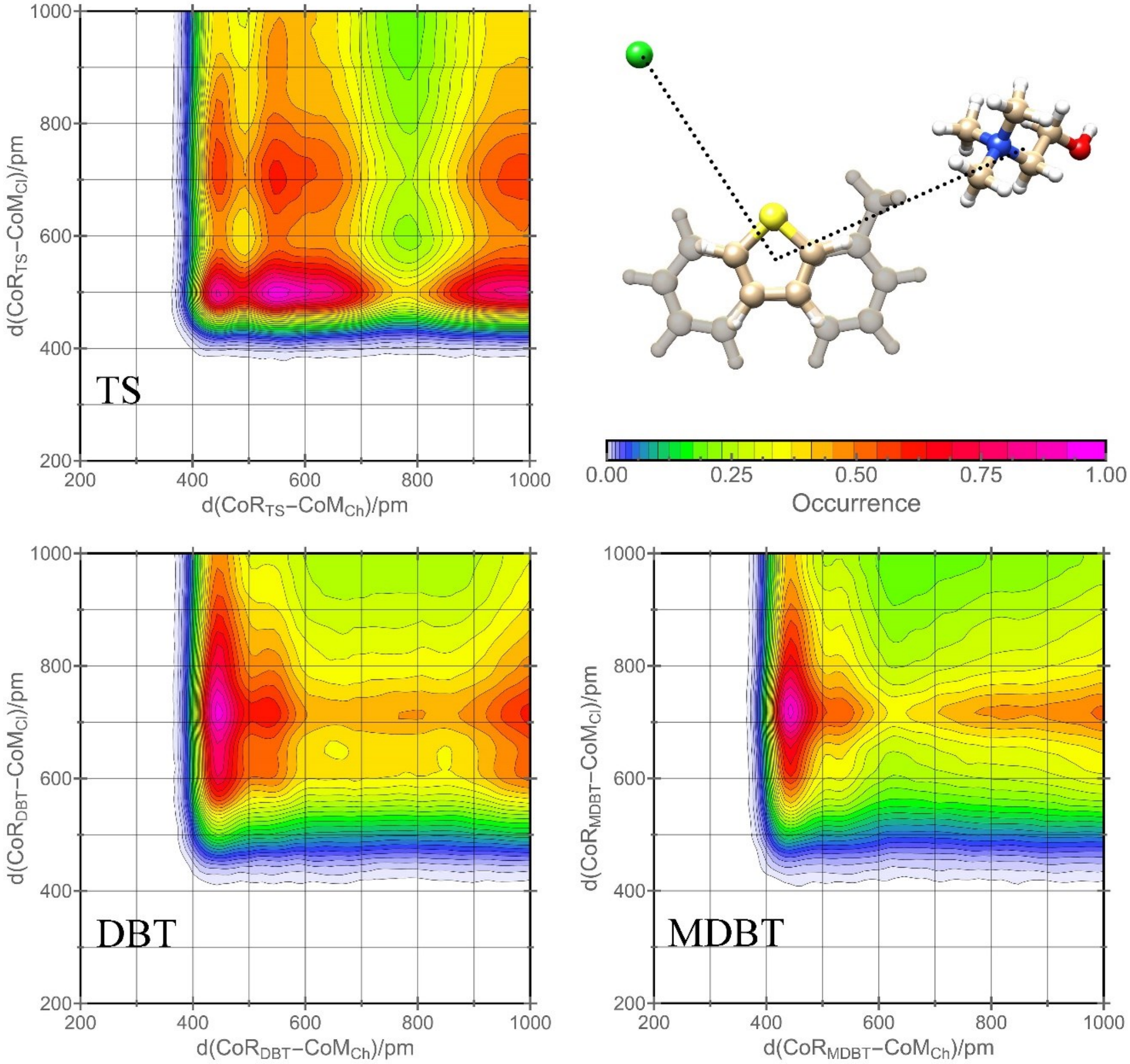

Figure 13. Combined distribution function (CDF) plots of the distance between the solute center-of-ring and the chloride center-of-mass, $d(\mathrm{CoR_{TS/DBT/MDBT}\text{-}CoM_{Cl}})$, versus the distance between the solute center-of-ring and the choline center-of-mass, $d(\mathrm{CoR_{TS/DBT/MDBT}\text{-}CoM_{Ch}})$. All distances in pm.

Analysis of the CCEtg systems using spatial distribution functions revealed the chloride anions to be evenly distributed around the edges of the TS and DBT compounds, i.e., perpendicular to the sulfur ring face, and adjacent to the hydrogen atoms (green color in Figure 14). However, a more asymmetrical distribution of Cl^- around MDBT was found with the anions avoiding the region near the methyl substituent. Interestingly, ethylene glycol also preferred to occupy similar locations as chloride, but at longer distances and primarily within the gape areas of the hydrogen atoms on the refractory sulfur compounds (magenta color in Figure 14). The SDFs indicated that the choline cations preferred to occupy the location over the TS/DBT/MDBT ring faces (blue color in Figure 14) in a similar fashion to the ILs despite lacking the π-π stacking ability of [BMIM]. Instead, the choline arrangement is perhaps driven by a cation-π interaction given the electron-rich region above and below the aromatic ring. For example, the experimental gas-phase ΔH binding energy of NMe_4^+ to benzene is a substantial 9.4 kcal/mol, which is comparable to a $NMe_4^+\cdots$water interaction.[95] The RDF, CDF, and SDF analyses of the CCEtg systems showed a consistent theme of synergistic electrostatic interactions between all the components of the DES, i.e., choline, ethylene glycol, and chloride, to solvate the refractory sulfur compounds with no dominant noncovalent interaction prevailing. Quantum chemical calculations of small clusters composed of a single refractory sulfur compound, e.g., BT and DBT, and 1:2 CCEtg or 1:2 choline chloride:urea (CCU) also reported multiple weak noncovalent interactions with Ch^+ and the HBDs but no direct interactions between the S-compounds and Cl$^-$.[96] An SDF analysis was performed for the CCGly/TS/DBT/MDBT systems and is provided in Figure S44. Many of the findings were comparable between CCGly and CCEtg, including cation-π interactions between the sulfur ring and choline, and chloride/glycerol compounds being located around the edges of the solutes near the hydrogen atoms. However, CCGly had a slightly more irregular configuration of ions/HBD around the solute as compared to CCEtg, which may be a consequence of the additional hydrogen bonding ability of glycerol that features three hydroxyl groups compared to two OH substituents for ethylene glycol (Scheme 3).

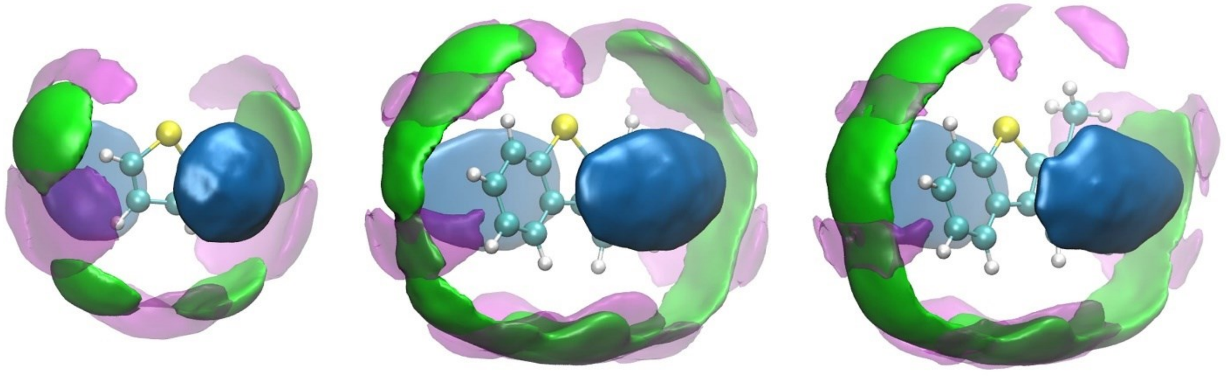

Figure 14. Spatial distribution functions (SDFs) of the choline cation (blue color), [Cl] anion (green color), and ethylene glycol (magenta color) around the TS/DBT/MDBT molecules from MD simulations.

The average coordination numbers (N_{coord}) for each individual solvent particle of CCEtg interacting with TS/DBT/MDBT are provided in Table 11 and were derived by integrating the area under the first peak from the center-of-mass RDF plots given in Figure S45 (CCGly/TS/DBT/MDBT data is provided in Table S39 and Figure S47). Solute size had a large influence on the computed N_{coord} solute-solvent interactions, particularly for the choline cations. For example, integration to the first peak minimum (r_{min}) values of 630 and 639 pm for Ch^+-DBT and Ch^+-MDBT, respectively, gave 2.1 and 2.2 choline cations coordinated to the corresponding sulfur compound. The maximum peak height distance (r_{max}) of 443-444 pm between Ch^+ and DBT/MDBT was mirrored in the most intense $d(\mathrm{CoR}_{\mathrm{DBT/MDBT}}\text{-}\mathrm{CoM}_{\mathrm{Ch}})$ occurrence region shown in the CDF plots (Figure 13). Conversely, the smaller thiophene compound yielded double the number of Ch^+ interactions (N_{coord} of 4.4) when integrated to a r_{min} of 780 pm (Table 11). This longer r_{min} distance for TS was also found in the CCEtg/TS CDF plot as the most intense interactions occurred over a wide $d(\mathrm{CoR}_{\mathrm{TS}}\text{-}\mathrm{CoM}_{\mathrm{Ch}})$ range of ~420-750 pm (Figure 13). The SDF analysis for CCEtg/TS showed the Ch^+ ions were preferentially located over the cyclic TS ring (Figure 14), but the large fluidity of the cations was reflected in the shorter and broader $g(r)$ peak between Ch^+-TS computed in the center-of-mass RDF plot (Figure S45). The DES hydrogen bond donors were also affected by the larger sizes of DBT and MDBT as they provided greater surface area for Etg interactions. Consequently, larger N_{coord} values of 12.0-12.6 Etg per DBT/MDBT were calculated compared to 8.0 Etg per TS (Table 11). Despite this, the TS-Etg interaction produced the largest $g(r)$ peak height of ~2.3 at the r_{max} of 519 pm, compared to $g(r)$ heights of ~1.7-1.8 for DBT/MDBT-Etg at longer r_{max} values of 586-595 pm (Figure S45). Interestingly, the interactions between chloride and the sulfur compounds were relatively similar for all systems with 10.8-11.2 Cl^- per TS/DBT/MDB, which further emphasized the anions' preference to form electrostatic interactions with other solvent components instead (Figure S46 and S48). In terms of the CCGly/TS/DBT/MDBT systems, peak distances and N_{coord} values from the center-of-mass RDF plots are provided in Figure S47 and Table S39. A solute size dependence was once again observed in the CCGly systems as the Ch^+ N_{coord} values were 4.1, 3.1, and 2.4 for TS, DBT, and MDBT, respectively (Table S39). Decreasing interactions with chloride also correlated to increasing solute size, i.e., Cl^- N_{coord} values of 5.9, 5.0, and 4.5 for TS, DBT, and MDBT, respectively. Curiously, increasing sulfur compound size led to a greater number of interactions with Gly, i.e., N_{coord} of 7.8, 9.7, and 11.8 with TS, DBT, and MDBT, respectively, perhaps a consequence of the additional hydroxyl group available on Gly compared to Etg (Scheme 3). Despite the effects that sulfur compound size had on the solute-solvent species interactions, the solvent-solvent r_{max}, r_{min}, and N_{coord} interactions for CCEtg and CCGly, i.e., between Ch^+, Cl^-, and Etg/Gly, were effectively identical in all systems (Tables S38 and S40 and Figures S46 and S48).

Table 11. Average coordination number (N_{coord}) and positions (pm) of the first maximum and first minimum in the center-of-mass RDFs between the TS/DBT/MDBT solutes and choline, chloride, and ethylene glycol from CCEtg.

		TS			**DBT**			**MDBT**		
Center	**Shell**	r_{max}	r_{min}	N_{Coord}	r_{max}	r_{min}	N_{Coord}	r_{max}	r_{min}	N_{Coord}
Solute	Ch^+	453	780[a]	4.4 ± 0.1	444	630[a]	2.1 ± 0.1	443	639[a]	2.2 ± 0.3
Solute	Cl^-	508	1035	11.2 ± 0.2	705	1031	10.8 ± 0.2	710	1025	11.1 ± 0.6
Solute	Etg	519	719	8.0 ± 0.1	586	838	12.0 ± 0.4	595	868	12.6 ± 0.3

[a] The integration of the convoluted peaks is applied to calculate the coordination number.

Conclusions

Simulations of five ILs, [BMIM][Cl], [BMIM][SCN], [BMIM][BF_4], [BMIM][PF_6], and [BMIM][NTf_2], and two DESs, CCEtg and CCGly, with three refractory sulfur compounds, TS, DBT, and MDBT, were carried out to analyze the intermolecular interactions and energies present between the solvents and aromatic sulfur compounds. Elucidating the role of solvent physiochemical properties, such as π-π interactions, anion volume, hydrophobic regions, hydrogen bonding, etc., on extraction potential was of particular importance. Initially, FEP-MD simulations were performed to calculate the excess chemical potentials ($\mu_i^{ex,\infty}$) of TS, DBT, and MDBT in all the ionic fluids studied. The IL/TS systems yielded computed $\mu_i^{ex,\infty}$ values comparable to experimental results with deviations of approximately 0.1-0.7 kcal/mol. The IL simulations revealed a trend that correlated more a favorable $\mu_i^{ex,\infty}$ energy to increasing anion size in line with reported experimental observations where the S-extraction efficiency of TS and DBT increased as [NTf_2] > [PF_6] > [BF_4] for [BMIM]-based ILs.[33] Accordingly, [BMIM][NTf_2] was computationally predicted to possess the strongest desulfurization potential for all three aromatic sulfur compounds. In terms of DESs, the $\mu_i^{ex,\infty}$ energies computed for the three cyclic S-compounds in the CCEtg and CCGly were higher in energy by approximately 1-3 kcal/mol than in the ILs. The reduced desulfurization potential of the DESs agreed with previous experimental examinations of CCEtg that yielded ~55% extraction efficiency of BT from *n*-octane[38] and 5% to 35% for TS from a model fuel.[86]

Radial, combined, and spatial distribution functions, (RDF, CDF, and SDF, respectively) were then used to determine which cation/anion/HBD interactions with the sulfur compounds were key to efficient desulfurization. An important conclusion from the RDF analysis of the IL systems was that the aromatic sulfur compounds had closer intermolecular distances and, presumably, stronger electrostatic/dispersion interactions with the anions rather than the cations. The present calculations corroborated *ab initio* MD simulations that found stronger energetic interactions present between TS and IL anions compared to the cations.[65] Interestingly, as the volume increased from the smaller [Cl] and [SCN] anions to the larger [BF_4], [PF_6], and [NTf_2] anions, the CDF and

SDF analysis showed the solute-anion interactions became more localized and structurally ordered. However, a significant π-π stacking interaction between the aromatic sulfur compounds and [BMIM] was found regardless of the anion present in the IL system highlighting the potential importance of this physical property to extraction ability. Interestingly, the current simulations also found noteworthy hydrogen bonding occurring between the most acidic proton on the [BMIM] ring, i.e., H2-C2 bisecting the nitrogen atoms, and the S-atom from the solute in the ILs with larger anions, i.e., [BMIM][PF_6] and [BMIM][NTf_2]. For example, the *g(r)* peak height between [BMIM]-H2 and S from DBT increased linearly with increasing anion size, that is, 0.69, 0.88, 1.07, 1.14, and 1.66 for [Cl], [SCN], [BF_4], [PF_6], and [NTf_2], respectively. The enhanced hydrogen bonding between the cation and solute may arise from weakened interactions between the IL ions themselves as anion volume increases.

The RDF, CDF, and SDF analyses of the DES systems showed a consistent theme of synergistic electrostatic interactions required from all solvent components, i.e., Ch^+, Cl^-, and Etg/Gly, to solvate the refractory sulfur compounds with no particularly dominant noncovalent interaction prevailing. The solvent organization of CCGly and CCEtg around the solutes were generally comparable, including cation-π interactions of Ch^+ above the plane of the aromatic sulfur ring with the remaining solvent species being located around the edges of the solutes near the hydrogen atoms. CCGly had a slightly more irregular configuration of ions/HBD around the solute as compared to CCEtg, which may be a consequence of the additional hydrogen bonding ability of Gly that possesses three hydroxyl groups compared to two OH moieties for Etg. The simulations did show some differences regarding solute size as the Ch^+ exhibited a larger fluidity featuring a wide interaction distance range of 420-700 pm with TS as compared to a more localized 440-460 pm region for DBT/MDBT. The long distances between Cl^- and TS/DBT/MDBT suggested very weak solute-solvent interactions, which was consistent with the stronger electrostatic interactions computed between Cl^- and Ch^+/HBD. Overall, the weaker DES solvation effects computed explain the modest experimental extraction efficiencies measured for choline chloride based DESs, suggesting that an alternative DES cation may be required for improved desulfurization of fuels.

Acknowledgement. Gratitude is expressed to the National Science Foundation (CHE-2102038) for support of this research. The authors appreciate the technical help provided by Dr. Marco Gallo in the calculation of excess chemical potentials.

Supporting Information Available: Mass, density, molar volume and γ_i^∞ values for the IL/TS systems; density of DESs; RDFs, CDFs, SDFs analyses, and average coordination numbers for TS, DBT, MDBT in [BMIM][Cl], [BMIM][SCN], [BMIM][BF_4], [BMIM][PF_6], and CCGly; The Supporting Information is available free of charge on the ACS Publications website at http://pubs.acs.org.

References

1. Regulatory Impact Analysis: Heavy-Duty Engine and Vehicle Standards and Highway Diesel Fuel Sulfur Control Requirements. EPA420-R-00-026, *United States Environmental Protection Agency*, **2000**.
2. Babich, I. V.; Moulijn, J. A., Science and technology of novel processes for deep desulfurization of oil refinery streams: a review. *Fuel* **2003,** *82*, 607-631.
3. Manisalidis, I.; Stavropoulou, E.; Stavropoulos, A.; Bezirtzoglou, E., Environmental and Health Impacts of Air Pollution: A Review. *Front. Public Health* **2020,** *8*, 14.
4. Curtis, L.; Rea, W.; Smith-Willis, P.; Fenyves, E.; Pan, Y., Adverse health effects of outdoor air pollutants. *Environ. Int.* **2006,** *32*, 815-830.
5. Srivastava, V. C., An Evaluation of Desulfurization Technologies for Sulfur Removal from Liquid Fuels. *RSC Adv.* **2012,** *2*, 759-783.
6. Song, C.; Ma, X., New design approaches to ultra-clean diesel fuels by deep desulfurization and deep dearomatization. *Appl. Catal. B* **2003,** *41*, 207-238.
7. Saleh, T. A., Characterization, determination and elimination technologies for sulfur from petroleum: Toward cleaner fuel and a safe environment. *Trends Environ. Anal. Chem.* **2020,** *25*, e00080.

8. Ma, X.; Sakanishi, K.; Mochida, I., Hydrodesulfurization reactivities of various sulfur compounds in diesel fuel. *Ind. Eng. Chem. Res.* **1994,** *33*, 218-222.
9. Prajapati, Y. N.; Verma, N., Hydrodesulfurization of Thiophene on Activated Carbon Fiber Supported NiMo Catalysts. *Energy Fuels* **2018,** *32*, 2183-2196.
10. Schuman, S. C.; Shalit, H., Hydrodesulfurization. *Catal. Rev.* **1971,** *4*, 245-318.
11. Schulz, H.; Böhringer, W.; Ousmanov, F.; Waller, P., Refractory sulfur compounds in gas oils. *Fuel Process. Technol.* **1999,** *61*, 5-41.
12. Tanimu, A.; Alhooshani, K., Advanced Hydrodesulfurization Catalysts: A Review of Design and Synthesis. *Energy Fuels* **2019,** *33*, 2810-2838.
13. Cui, T.-Y.; Rajendran, A.; Fan, H.-X.; Feng, J.; Li, W.-Y., Review on Hydrodesulfurization over Zeolite-Based Catalysts. *Ind. Eng. Chem. Res.* **2021,** *60*, 3295-3323.
14. Toutov, A. A.; Salata, M.; Fedorov, A.; Yang, Y.-F.; Liang, Y.; Cariou, R.; Betz, K. N.; Couzijn, E. P. A.; Shabaker, J. W.; Houk, K. N.; Grubbs, R. H., A potassium tert-butoxide and hydrosilane system for ultra-deep desulfurization of fuels. *Nature Energy* **2017,** *2*, 17008.
15. Ho, T. C., Deep HDS of diesel fuel: chemistry and catalysis. *Cat. Today* **2004,** *98*, 3-18.
16. Kadhum, A. T.; Albayati, T. M., Desulfurization techniques process and future challenges for commercial of crude oil products: Review. *AIP Conference Proceedings* **2022,** *2443*, 030039.
17. Song, C., An overview of new approaches to deep desulfurization for ultra-clean gasoline, diesel fuel and jet fuel. *Cat. Today* **2003,** *86*, 211-263.
18. Mohebali, G.; Ball, A. S., Biocatalytic desulfurization (BDS) of petrodiesel fuels. *Microbiology* **2008,** *154*, 2169-2183.
19. Soleimani, M.; Bassi, A.; Margaritis, A., Biodesulfurization of refractory organic sulfur compounds in fossil fuels. *Biotechnol. Adv.* **2007,** *25*, 570-596.
20. McFarland, B. L., Biodesulfurization. *Curr. Opin. Microbiol.* **1999,** *2*, 257-264.
21. Gray, K. A.; Mrachko, G. T.; Squires, C. H., Biodesulfurization of fossil fuels. *Curr. Opin. Microbiol.* **2003,** *6*, 229-235.
22. Omar, R. A.; Verma, N., Review of Adsorptive Desulfurization of Liquid Fuels and Regeneration Attempts. *Ind. Eng. Chem. Res.* **2022,** *61*, 8595-8606.
23. Mjalli, F. S.; Ahmed, O. U.; Al-Wahaibi, T.; Al-Wahaibi, Y.; AlNashef, I. M., Deep oxidative desulfurization of liquid fuels. *Rev. Chem. Eng.* **2014,** *30*, 337-378.
24. Campos-Martin, J. M.; Capel-Sanchez, M. C.; Perez-Presas, P.; Fierro, J. L. G., Oxidative Processes of Desulfurization of Liquid Fuels. *J. Chem. Technol. Biotechnol.* **2010,** *85*, 879-890.
25. Abro, R.; Abdeltawab, A. A.; Al-Deyab, S. S.; Yu, G.; Qazi, A. B.; Gao, S.; Chen, X., A review of extractive desulfurization of fuel oils using ionic liquids. **2014,** *4*, 35302-35317.
26. Katasonova, O. N.; Savonina, E. Y.; Maryutina, T. A., Extraction Methods for Removing Sulfur and Its Compounds from Crude Oil and Petroleum Products. *Russ. J. Appl. Chem.* **2021,** *94*, 441-436.
27. Pena-Pereira, F.; Namieśnik, J., Ionic Liquids and Deep Eutectic Mixtures: Sustainable Solvents for Extraction Processes. *ChemSusChem* **2014,** *7*, 1784-1800.
28. Bösmann, A.; Datsevich, A.; Jess, A.; Lauter, C.; Schmitz, C.; Wasserscheid, P., Deep desulfurization of diesel fuel by extraction with ionic liquids. *Chem. Commun.* **2001**, 2494-2495.
29. Eßer, J.; Wasserscheid, P.; Jess, A., Deep desulfurization of oil refinery streams by extraction with ionic liquids. *Green Chem.* **2004,** *6*, 316-322.
30. Francisco, M.; Arce, A.; Soto, A., Ionic liquids on desulfurization of fuel oils. *Fluid Phase Equilib.* **2010,** *294*, 39-48.

31. Kulkarni, P. S.; Afonso, C. A. M., Deep desulfurization of diesel fuel using ionic liquids: current status and future challenges. *Green Chem.* **2010,** *12*, 1139-1149.
32. Hosseini, A.; Khoshsima, A.; Sabzi, M.; Rostam, A., Toward Application of Ionic Liquids to Desulfurization of Fuels: A Review. *Energy Fuels* **2022,** *36*, 4119-4152.
33. Player, L. C.; Chan, B.; Lui, M. Y.; Masters, A. F.; Maschmeyer, T., Toward an Understanding of the Forces Behind Extractive Desulfurization of Fuels with Ionic Liquids. *ACS Sustainable Chem. Eng.* **2019,** *7*, 4087-4093.
34. Ibrahim, M. H.; Hayyan, M.; Hashim, M. A.; Hayyan, A., The role of ionic liquids in desulfurization of fuels: A review. *Renew. Sust. Energy Rev.* **2017,** *76*, 1534-1549.
35. Abbott, A. P.; Capper, G.; Davies, D. L.; Rasheed, R. K.; Tambyrajah, V., Novel solvent properties of choline chloride/urea mixtures. *Chem. Commun.* **2003**, *1*, 70-71.
36. Abbott, A. P.; Boothby, D.; Capper, G.; Davies, D. L.; Rasheed, R. K., Deep eutectic solvents formed between choline chloride and carboxylic acids: versatile alternatives to ionic liquids. *J. Am. Chem. Soc.* **2004,** *126*, 9142-7.
37. Smith, E. L.; Abbott, A. P.; Ryder, K. S., Deep Eutectic Solvents (DESs) and Their Applications. *Chem. Rev.* **2014,** *114*, 11060–11082.
38. Li, C.; Li, D.; Zou, S.; Li, Z.; Yin, J.; Wang, A.; Cui, Y.; Yao, Z.; Zhao, Q., Extraction desulfurization process of fuels with ammonium-based deep eutectic solvents. *Green Chem.* **2013,** *15*, 2793-2799.
39. Abro, R.; Kiran, N.; Ahmed, S.; Muhammad, A.; Jatoi, A. S.; Mazari, S. A.; Salma, U.; Plechkova, N. V., Extractive desulfurization of fuel oils using deep eutectic solvents – A comprehensive review. *J. Environ. Chem. Eng.* **2022,** *10*, 107369.
40. Lima, F.; Branco, L. C.; Silvestre, A. J. D.; Marrucho, I. M., Deep desulfurization of fuels: Are deep eutectic solvents the alternative for ionic liquids? *Fuel* **2021,** *293*, 120297.
41. Tahir, S.; Qazi, U. Y.; Naseem, Z.; Tahir, N.; Zahid, M.; Javaid, R.; Shahid, I., Deep eutectic solvents as alternative green solvents for the efficient desulfurization of liquid fuel: a comprehensive review. *Fuel* **2021,** *305*, 121502.
42. Chandran, D.; Khalid, M.; Walvekar, R.; Mubarak, N. M.; Dharaskar, S.; Wong, W. Y.; Gupta, T. C. S. M., Deep eutectic solvents for extraction-desulphurization: A review. *J. Mol. Liq.* **2019,** *275*, 312-322.
43. Velez, C.; Acevedo, O., Simulation of Deep Eutectic Solvents: Progress to Promises. *WIREs Comput. Mol. Sci.* **2022**, *12*, e1598.
44. Rukmani, S. J.; Doherty, B.; Acevedo, O.; Colina, C. M., Molecular simulations of deep eutetic solvents: A perspective on structure, dynamics, and physical properties. *Rev. Comput. Chem.* **2022,** *32*, 135-216.
45. Kumar, A. A. P.; Banerjee, T., Separation with Ionic Liquids for Desulphurization : A Quantum Chemical Approach. *Fluid Phase Equilib.* **2009,** *278*, 1-8.
46. Wilfred, C. D.; Man, Z.; Chan, Z. P., Predicting Methods for Sulfur Removal from Model Oils Using COSMO-RS and Partition Coefficient. *Chem. Eng. Sci.* **2013,** *102*, 373–377.
47. Song, Z.; Zhou, T.; Qi, Z.; Sundmacher, K., Systematic Method for Screening Ionic Liquids as Extraction Solvents Exempli Fi Ed by an Extractive Desulfurization Process. *ACS Sustain. Chem. Eng.* **2017,** *5*, 3382−3389.
48. Cheng, H.; Liu, C.; Zhang, J.; Chen, L.; Zhang, B.; Qi, Z., Screening deep eutectic solvents for extractive desulfurization of fuel based on COSMO-RS model. *Chem. Eng. Process.* **2018,** *125*, 246-252.

49. Yuan, P.; Zhang, T. T.; Cai, A. F.; Cui, C. S.; Liu, H. Y.; Bao, X. J., Theoretical study on the mechanism of oxidative–extractive desulfurization in imidazolium-based ionic liquid. *RSC Adv.* **2016,** *6*, 74929-74936.

50. Liu, X.; Zhou, G.; Zhang, X.; Zhang, S., Molecular Dynamics Simulation of Desulfurization by Ionic Liquids. *AIChE J.* **2010,** *56*, 2983–2996.

51. Singh, M. B.; Harmalkar, A. U.; Prabhu, S. S.; Pai, N. R.; Bhangde, S. K.; Gaikar, V. G., Molecular dynamics simulation for desulphurization of hydrocarbon fuel using ionic liquids. *J. Mol. Liq.* **2018,** *264*, 490-498.

52. Zeng, Y.; Jin, J.; Wang, C.; Xu, Y.; Wang, J.; Ju, S., Monte Carlo simulations of phase equilibria and microstructure of thiophene/[Bmim][PF6]/CO2. *Chem. Eng. Sci.* **2016,** *149*, 88-96.

53. Sambasivarao, S. V.; Acevedo, O., Development of OPLS-AA Force Field Parameters for 68 Unique Ionic Liquids. *J. Chem. Theory Comput.* **2009,** *5*, 1038-1050.

54. Doherty, B.; Zhong, X.; Gathiaka, S.; Li, B.; Acevedo, O., Revisiting OPLS Force Field Parameters for Ionic Liquid Simulations. *J. Chem. Theory Comput.* **2017,** *13*, 6131-6145.

55. Doherty, B.; Zhong, X.; Acevedo, O., Virtual Site OPLS Force Field for Imidazolium-Based Ionic Liquids. *J. Phys. Chem. B* **2018,** *122*, 2962-2974.

56. Velez, C.; Doherty, B.; Acevedo, O., Accurate Diels-Alder Energies and Endo Selectivity in Ionic Liquids using the OPLS-VSIL Force Field. *Int. J. Mol. Sci.* **2020,** *21*, 1190.

57. Yue, K.; Doherty, B.; Acevedo, O., Comparison between Ab Initio Molecular Dynamics and OPLS-Based Force Fields for Ionic Liquid Solvent Organization. *J. Phys. Chem. B* **2022,** *126*, 3908-3919.

58. Doherty, B.; Acevedo, O., OPLS Force Field for Choline Chloride-Based Deep Eutectic Solvents. *J. Phys. Chem. B* **2018,** *122*, 9982-9993.

59. Zhong, X.; Velez, C.; Acevedo, O., Partial Charges Optimized by Genetic Algorithms for Deep Eutectic Solvent Simulations. *J. Chem. Theory Comput.* **2021,** *17*, 3078-3087.

60. Dodda, L. S.; Cabeza de Vaca, I.; Tirado-Rives, J.; Jorgensen, W. L., LigParGen Web Server : An Automatic OPLS-AA Parameter Generator for Organic Ligands. *Nucleic Acids Res.* **2017,** *45*, W331–W336.

61. Abraham, M. J.; Murtola, T.; Schulz, R.; Páll, S.; Smith, J. C.; Hess, B.; Lindahl, E., GROMACS: High performance molecular simulations through multi-level parallelism from laptops to supercomputers. *SoftwareX* **2015,** *1-2*, 19-25.

62. Martínez, L.; Andrade, R.; Birgin, E. G.; Martínez, J. M., Packmol: A package for building initial configurations for molecular dynamics simulations. *J. Comput. Chem.* **2009,** *30*, 2157-2164.

63. Brehm, M.; Thomas, M.; Gehrke, S.; Kirchner, B., TRAVIS—A free analyzer for trajectories from molecular simulation. *J. Chem. Phys.* **2020,** *152*, 164105.

64. Brehm, M.; Kirchner, B., TRAVIS - a free analyzer and visualizer for Monte Carlo and molecular dynamics trajectories. *J. Chem. Inf. Model.* **2011,** *51*, 2007-2023.

65. Velarde-Salcedo, M. V.; Sánchez-Badillo, J.; Gallo, M.; Jorge López-Lemus, J., Excess chemical potential of thiophene in [C_4MIM] [BF_4, Cl, Br, CH_3COO] ionic liquids, determined by molecular simulations. *RSC Adv.* **2021,** *11*, 29394-29406.

66. Bennett, C. H., Efficient estimation of free energy differences from Monte Carlo data. *J. Comput. Phys.* **1976,** *22*, 245-268.

67. Van Gunsteren, W. F.; Berendsen, H. J. C., A Leap-frog Algorithm for Stochastic Dynamics. *Mol. Simul.* **1988,** *1*, 173-185.

68. Klimovich, P. V.; Shirts, M. R.; Mobley, D. L., Guidelines for the analysis of free energy calculations. *J. Comput. Aided Mol. Des.* **2015,** *29*, 397-411.

69. Lindahl, E.; Abraham, M. J.; Hess, B.; van der Spoel, D., GROMACS 2021.6 Manual, Zenodo, 2022.

70. Beutler, T. C.; Mark, A. E.; van Schaik, R. C.; Greber, P. R.; van Gunsteren, W. F., Avoiding singularities and numerical instabilities in free energy calculations based on molecular simulations. *Chem. Phys. Lett.* **1994,** *222*, 529-539.

71. Matos, G. D. R.; Kyu, D. Y.; Loeffler, H. H.; Chodera, J. D.; Shirts, M. R.; Mobley, D. L., Approaches for Calculating Solvation Free Energies and Enthalpies Demonstrated with an Update of the FreeSolv Database. *J. Chem. Eng. Data* **2017,** *62*, 1559-1569.

72. Dhakal, P.; Roese, S. N.; Stalcup, E. M.; Paluch, A. S., Application of MOSCED To Predict Limiting Activity Coefficients, Hydration Free Energies, Henry's Constants, Octanol/Water Partition Coefficients, and Isobaric Azeotropic Vapor−Liquid Equilibrium. *J. Chem. Eng. Data* **2018,** *63*, 352-364.

73. Alessi, P.; Fermeglia, M.; Kikic, I., Significance of dilute regions. *Fluid Phase Equilib.* **1991,** *70*, 239-250.

74. Brouwer, T.; Schuur, B., Model Performances Evaluated for Infinite Dilution Activity Coefficients Prediction at 298.15 K. *Ind. Eng. Chem. Res.* **2019,** *58*, 8903-8914.

75. Martins, M. A. R.; Coutinho, J. A. P.; Pinho, S. P.; Doman, U., Measurements of activity coefficients at infinite dilution of organic solutes and water on polar imidazolium-based ionic liquids. *J. Chem. Thermodyn.* **2015,** *91*, 194-203.

76. Domańska, U.; Laskowska, M., Measurements of activity coefficients at infinite dilution of aliphatic and aromatic hydrocarbons, alcohols, thiophene, tetrahydrofuran, MTBE, and water in ionic liquid [BMIM][SCN] using GLC. *J. Chem. Thermodyn.* **2009,** *41*, 645-650.

77. Revelli, A.-L.; Mutelet, F.; Turmine, M.; Solimando, R.; Jaubert, J.-N., Activity Coefficients at Infinite Dilution of Organic Compounds in 1-Butyl-3-methylimidazolium Tetrafluoroborate Using Inverse Gas Chromatography. *J. Chem. Eng. Data* **2009,** *54*, 90-101.

78. Zhang, J.; Zhang, Q.; Qiao, B.; Deng, Y., Solubilities of the Gaseous and Liquid Solutes and Their Thermodynamics of Solubilization in the Novel Room-Temperature Ionic Liquids at Infinite Dilution by Gas Chromatography. *J. Chem. Eng. Data* **2007,** *52*, 2277-2283.

79. Mutelet, F.; Butet, V.; Jaubert, J.-N., Application of Inverse Gas Chromatography and Regular Solution Theory for Characterization of Ionic Liquids. *Ind. Eng. Chem. Res.* **2005,** *44*, 4120-4127.

80. Xu, Q.; Su, B.; Luo, X.; Xing, H.; Bao, Z.; Yang, Q.; Yang, Y.; Ren, Q., Accurate measurements of infinite dilution activity coefficients using gas chromatography with static-wall-coated open-tubular columns. *Anal. Chem.* **2012,** *84*, 9109-9115.

81. Mutelet, F.; Baker, G. A.; Ravula, S.; Qian, E.; Wang, L.; Acree Jr, W. E., Infinite dilution activity coefficients and gas-to-liquid partition coefficients of organic solutes dissolved in 1-sec-butyl-3-methylimidazolium bis(trifluoromethylsulfonyl)imide and in 1-tert-butyl-3-methylimidazolium bis(trifluoromethylsulfonyl)imide. *Phys. Chem. Liq.* **2019,** *57*, 453-472.

82. Paduszyński, K., In Silico Calculation of Infinite Dilution Activity Coefficients of Molecular Solutes in Ionic Liquids: Critical Review of Current Methods and New Models Based on Three Machine Learning Algorithms. *J. Chem. Inf. Model.* **2016,** *56*, 1420-1437.

83. Griffin, P.; Ramer, S.; Winfough, M.; Kostal, J., Practical guide to designing safer ionic liquids for cellulose dissolution using a tiered computational framework. *Green Chem.* **2020,** *22*, 3626-3637.

84. Zhang, S.; Zhang, Q.; Zhang, Z. C., Extractive Desulfurization and Denitrogenation of Fuels Using Ionic Liquids. *Ind. Eng. Chem. Res.* **2004,** *43*, 614-622.

85. Lui, M. Y.; Cattelan, L.; Player, L. C.; Masters, A. F.; Perosa, A.; Selva, M.; Maschmeyer, T., Extractive Denitrogenation of Fuel Oils with Ionic Liquids: A Systematic Study. *Energy Fuels* **2017,** *31*, 2183-2189.
86. Rogošić, M.; Kučan, K. Z., Deep eutectic solvents based on choline chloride and ethylene glycol as media for extractive denitrification/desulfurization/dearomatization of motor fuels. *J. Ind. End. Chem.* **2019,** *72*, 87-99.
87. Kempter, V.; Kirchner, B., The role of hydrogen atoms in interactions involving imidazolium-based ionic liquids. *J. Mol. Struct.* **2010,** *972*, 22-34.
88. Peppel, T.; Roth, C.; Fumino, K.; Paschek, D.; Kockerling, M.; Ludwig, R., The Influence of Hydrogen-Bond Defects on the Properties of Ionic Liquids. *Angew. Chem. Int. Ed.* **2011,** *50*, 6661–6665.
89. Thar, J.; Brehm, M.; Seitsonen, A. P.; Kirchner, B., Unexpected Hydrogen Bond Dynamics in Imidazolium-Based Ionic Liquids. *J. Phys. Chem. B* **2009,** *113*, 15129–15132.
90. Weber, H.; Hollóczki, O.; Pensado, A. S.; Kirchner, B., Side chain fluorination and anion effect on the structure of 1-butyl-3-methylimidazolium ionic liquids. *J. Chem. Phys.* **2013,** *139*, 084502.
91. Matthews, R. P.; Welton, T.; Hunt, P. A., Hydrogen bonding and π–π interactions in imidazolium-chloride ionic liquid clusters. *Phys. Chem. Chem. Phys.* **2015,** *17*, 14437-14453.
92. Matthews, R. P.; Villar-Garcia, I. J.; Weber, C. C.; Griffith, J.; Cameron, F.; Hallett, J. P.; Hunt, P. A.; Welton, T., A structural investigation of ionic liquid mixtures. *Phys. Chem. Chem. Phys.* **2016,** *18*, 8608-8624.
93. Oliveira, O. V.; Paluch, A. S.; Costa, L. T., A molecular understanding of the phase-behavior of thiophene in the ionic liquid $[C_4mim]^+[BF_4]^-$ for extraction from petroleum streams. *Fuel* **2016,** *175*, 225-231.
94. Wilfred, C. D.; Kiat, C. F.; Man, Z.; Bustam, M. A.; Mutalib, M. I. M.; Phak, C. Z., Extraction of dibenzothiophene from dodecane using ionic liquids. *Fuel Process. Technol.* **2012,** *93*, 85-89.
95. Ma, J. C.; Dougherty, D. A., The Cation−π Interaction. *Chem. Rev.* **1997,** *97*, 1303-1324.
96. Wagle, D. V.; Zhao, H.; Deakyne, C. A.; Baker, G. A., Quantum Chemical Evaluation of Deep Eutectic Solvents for the Extractive Desulfurization of Fuel. *ACS Sustainable Chem. Eng.* **2018,** *6*, 7525-7531.

TOC Graphic

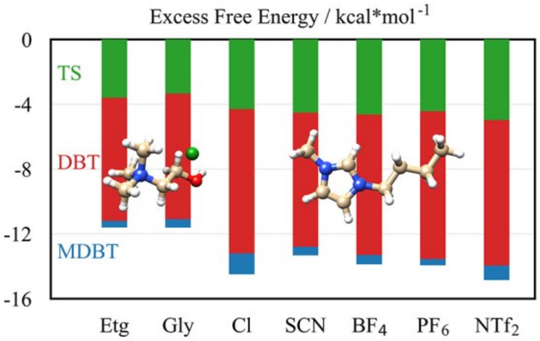
Excess Free Energy / kcal*mol-1
0
-4
-8
-12
-16
TS
DBT
MDBT
N
N
N
Etg
Gly
Cl
SCN
BF4
PF6
NTf2